Physica D 241 (2012) 1680–1702

Contents lists available at SciVerse ScienceDirect

Physica D

journal homepage: www.elsevier.com/locate/physd

Geodesic theory of transport barriers in two-dimensional flows

George Haller [a,b,*], Francisco J. Beron-Vera [c]

[a] *Department of Mechanical Engineering, McGill University, 817 Sherbrooke Ave. West, Montreal, Quebec H3A 2K6, Canada*
[b] *Department of Mathematics and Statistics, McGill University, 817 Sherbrooke Ave. West, Montreal, Quebec H3A 2K6, Canada*
[c] *Rosenstiel School of Marine and Atmospheric Science, University of Miami, 4600 Rickenbacker Cswy., Miami, FL 33149, USA*

ARTICLE INFO

Article history:
Received 25 January 2012
Received in revised form
6 June 2012
Accepted 21 June 2012
Available online 27 July 2012
Communicated by J. Dawes

Keywords:
Transport
Coherent structures
Non-autonomous dynamical systems
Manifolds
Invariant tori

ABSTRACT

We introduce a new approach to locating key material transport barriers in two-dimensional, non-autonomous dynamical systems, such as unsteady planar fluid flows. Seeking transport barriers as minimally stretching material lines, we obtain that such barriers must be shadowed by minimal geodesics under the Riemannian metric induced by the Cauchy–Green strain tensor. As a result, snapshots of transport barriers can be explicitly computed as trajectories of ordinary differential equations. Using this approach, we locate hyperbolic barriers (generalized stable and unstable manifolds), elliptic barriers (generalized KAM curves) and parabolic barriers (generalized shear jets) in temporally aperiodic flows defined over a finite time interval. Our approach also yields a metric (geodesic deviation) that determines the minimal computational time scale needed for a robust numerical identification of generalized Lagrangian Coherent Structures (LCSs). As we show, an extension of our transport barrier theory to non-Euclidean flow domains, such as a sphere, follows directly. We illustrate our main results by computing key transport barriers in a chaotic advection map, and in a geophysical model flow with chaotic time dependence.

1. Introduction

Most dynamical systems with general time dependence have no classic phase space barriers, such as periodic and quasiperiodic orbits, or homoclinic and heteroclinic trajectories. Yet, even in such general systems, the observed lack of exchange among flow domains often suggests the presence of generalized transport barriers. Here we develop an approach to uncover such barriers in two-dimensional flows.

There is broad interest in identifying, forecasting or even controlling transport barriers in a number of physical settings, including geophysical flows [1], chemical mixers [2], celestial mechanics [3], molecular reaction dynamics [4], and nuclear fusion [5]. Despite this widespread interest, however, a universal defining property of transport barriers has not emerged.

Indeed, while it is often noted that the flux through a transport barrier is expected to be zero or near-zero, the flux through *any* material line (an evolving curve of initial conditions) will also be zero. Admittedly, in autonomous or time-periodic dynamical systems, one may exclude unsteady or temporally aperiodic material lines from consideration, and define transport barriers as steady material lines (invariant curves) for the flow or for the associated Poincaré map. In aperiodic dynamical systems, however, no material lines are expected to remain steady under the flow or under any stroboscopic mapping, and hence imposing steadiness as a distinguishing property of barriers is not a viable option. In turn, zero flux as a defining property of transport barriers becomes meaningless for dynamical systems with general time dependence.

Beyond lacking a general definition, the study of transport barriers has also been more heuristic than analytic in nature. A number of Eulerian (i.e, lab-frame based) and Lagrangian (i.e., trajectory-based) diagnostic tools have been proposed to highlight barriers (see [6–9] for reviews). Careful studies of these diagnostics, however, tend to reveal shortcomings, including dependence on the reference frame and threshold parameters [10,6,8], as well as the accidental detection of structures with large flux as barriers [11]. More recent set-theoretical and topological approaches bring a much needed mathematical flavor to the subject area [12,13], but focus more on detecting the sets separated by transport barriers. As a result, these approaches have proven less efficient in locating the barriers themselves.

Here we propose an approach to describe transport barriers as exceptional material lines that deform less than their neighbors. This minimal stretching property is readily verified for all canonical examples of barriers in two dimensions, including stable and unstable manifolds of steady fixed points, steady shear jets, and

* Correspondence to: Institute for Mechanics, ETH Zürich, CLA J.26, Tannenstrasse 3, 8092 Zürich, Switzerland. Tel.: +41 44 633 82 50; fax: +41 44 632 11 45.
E-mail address: georgehaller@ethz.ch (G. Haller).

0167-2789/$ – see front matter © 2012 Elsevier B.V. All rights reserved.
doi:10.1016/j.physd.2012.06.012

KAM curves in time-periodic flows. We take this extremum property as a definition of transport barriers, and build a variational theory that identifies the most influential barriers in general unsteady flows. This theory represents a generalization of the concept of Lagrangian Coherent Structures (LCSs) from hyperbolic material lines [11] to elliptic and parabolic material lines.

Our minimal stretching approach ultimately leads to first-order differential equations for hyperbolic and shear-type transport barriers. The differential equations represent dynamical systems that are dual to the original time-evolving flow: their trajectories are snapshots of influential material lines in the phase space at a frozen time instance. These influential material lines, which we call *strainlines* and *shearlines*, turn out to act as strong transport barriers whenever they run close to least-stretching geodesics of the metric induced by the Cauchy–Green strain tensor, a classic positive definite tensor field used in describing the deformation of moving continua [14,2].[1] The Cauchy–Green metric is defined on the space of initial fluid particle positions; accordingly, strainlines and shearlines mark the initial positions of the transport barriers. Later positions of these barriers can be identified by advecting them under the flow map.

Closeness to least-stretching geodesics is measured in terms of the *geodesic deviation*, the pointwise C^2-distance of a curve from the most shrinking Cauchy–Green geodesic through the same point. Use of the geodesic deviation allows for the optimization of numerical barrier extraction. Specifically, the integration of trajectories for transport barrier analysis can be stopped once the geodesic deviation on strainlines and shearlines drops below a desired error bar. This procedure provides a long-sought answer to a question in Lagrangian structure extraction: How long should one integrate to obtain converged Lagrangian structures in a time-aperiodic data set?

We illustrate the geodesic transport theory developed here on simple analytic model flows, then on a discrete advection mapping with well-understood barriers. Surprisingly, our theory identifies elliptic barriers from data sets that are significantly shorter than what is normally needed to visualize KAM curves with the same resolution. Next, we uncover transport barriers in a meandering jet model perturbed in a temporally chaotic fashion. In this case, invariant manifold theory, KAM theory or Poincaré maps do not apply, and hence the direct detection – or even the indirect visualization – of barriers has been an open problem. In Appendix G, we also describe an extension of our theory to non-Euclidean flow domains, such as the surface of a planet.

2. Motivation: Simple examples of transport barriers

Consider the planar dynamical system

$$\dot{x} = v(x,t), \quad x \in U \subset \mathbb{R}^2,\ t \in [t_-, t_+]\,, \tag{1}$$

defined by the smooth vector field v on an open spatial domain U, and over the finite time interval $[t_-, t_+]$. The flow map for (1) is defined between initial times t_0 and final times t within $[t_-, t_+]$ as

$$F_{t_0}^t(x_0) := x(t; t_0, x_0),$$

with $x(t; t_0, x_0)$ denoting the solution of (1) starting at time t_0 from the position x_0.

Consider a smooth, parametrized curve of initial conditions

$$\gamma_0 = \{x_0 = r(s) \subset U : s \in [s_1, s_2]\}\,,$$

[1] The *least-stretching geodesic* at a point p is the geodesic tangent to the direction of minimal stretching at p. This direction is the eigenvector corresponding to the smaller eigenvalue of the Cauchy–Green strain tensor.

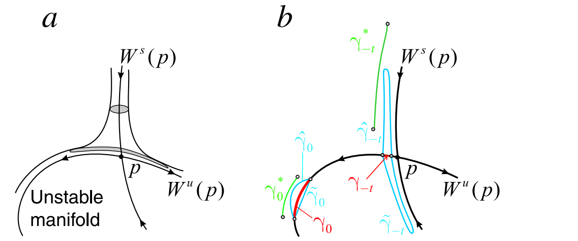

Fig. 1. (a) Unstable manifold $W^u(p)$ of a saddle p, observed as a transport barrier in forward time. (b) Minimal stretching property of a curve $\gamma_0 \subset W^u(p)$ in large enough backward time, relative to the nearby initial curves $\hat{\gamma}_0$, $\tilde{\gamma}_0$, and γ_0^*. Note that γ_{-t} is shorter than $\tilde{\gamma}_{-t}$, even though γ_0 was initially shorter than $\tilde{\gamma}_0$. Observe that the extremum property of γ_0 also holds with respect to nearby curves of the unstable manifold, such as γ_0^*, that do not even share their endpoints with γ_0.

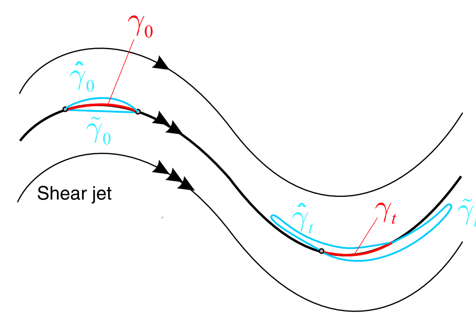

Fig. 2. Minimal stretching property of a material line, for large enough times, in a steady meandering jet among material lines with the same endpoints. Note that perturbations to the curve γ_0 will stretch longer than γ_t, whether or not they were initially longer than γ_0.

with its endpoints $a = r(s_1)$ and $b = r(s_2)$ yet unspecified. The curve γ_0 is carried forward by the flow map into a time-evolving material line

$$\gamma_t = F_{t_0}^t(\gamma_0)\,. \tag{2}$$

In three classic examples of transport barriers, we now point out a common minimal stretching property that a material line γ_t must possess to be observed as a transport barrier.

Example 1: Stable and unstable manifolds of a saddle point in steady flow

Finite material lines in stable and unstable manifolds of saddle points show minimal stretching relative to nearby material lines that are not subsets of the manifolds (see Fig. 1). The latter class of material lines stretches more due to normal repulsion by the underlying manifold in forward or backward time.

Example 2: Shear jet in steady flow

A reference material line within a jet trajectory shows minimal stretching relative to nearby material lines that share their endpoints with the reference material line (see Fig. 2). The latter class of material lines stretch more due to strong shear along the underlying jet trajectory. At each point of the jet, an appropriately defined Lagrangian measure of shear is maximal along the direction of the jet (see Appendix A).

Example 3: KAM curve in incompressible, time-periodic flow

A reference material line within a KAM curve – a closed invariant curve of the period-T map – shows minimal stretching relative to nearby material lines that share their endpoints with the reference material line (Fig. 3). The latter class of material lines

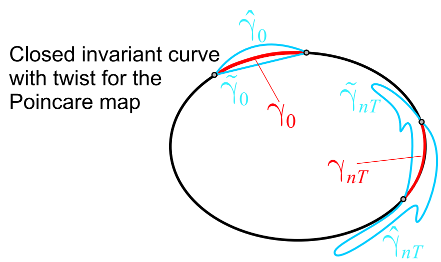

Fig. 3. Minimal stretching property for a closed transport barrier (a KAM curve) in a two-dimensional temporally T-periodic flow, for large enough iteration numbers n of the Poincare map. Note that fixed-endpoint perturbations to the curve γ_0 will stretch longer than γ_{nT}, whether or not they were initially longer than γ_0.

stretches more due to strong shear (twist) across the KAM curve. The KAM curve preserves its length under the period-T map.

The simple properties reviewed in this section for well-known steady and time-periodic flows will guide us in the development of a general theory for transport barriers in two-dimensional unsteady flows given over finite time intervals.

3. Transport barriers as material length minimizers

In a well-mixed flow, most material lines stretch, typically at an exponential rate. We seek transport barriers as exceptional material lines that defy this trend by being the locally least stretching material lines in forward or backward time. Transport barriers identified in this fashion are automatically frame-independent (or objective) and invariant under the flow (or Lagrangian, in fluid mechanical terms). The three canonical examples of transport barriers we discussed in Section 2 all share this minimal stretching property, but also exhibit subtle differences that we shall exploit in our analysis.

3.1. Formulation

An evolving material line γ_t, as defined in (2), has length

$$l(\gamma_t) = \int_{\gamma_t} |dx| = \int_a^b \left|DF_{t_0}^t(r)dr\right| = \int_{s_1}^{s_2} \sqrt{\langle r', C_{t_0}^t(r)r'\rangle} ds, \tag{3}$$

where $DF_{t_0}^t(x_0)$ denotes the derivative of the flow map, and

$$C_{t_0}^t = \left(DF_{t_0}^t\right)^T DF_{t_0}^t \tag{4}$$

denotes the Cauchy–Green strain tensor, with T referring to the matrix transpose.

The eigenvalues $\lambda_i(x_0)$ and unit eigenvectors $\xi_i(x_0)$ of the positive definite, symmetric tensor $C_{t_0}^t(x_0)$ satisfy

$$C_{t_0}^t \xi_i = \lambda_i \xi_i, \qquad |\xi_i| = 1, \quad i = 1, 2, \; 0 < \lambda_1 \le \lambda_2. \tag{5}$$

We will only be considering initial points x_0 with $\lambda_1(x_0) \neq \lambda_2(x_0)$, which are generically isolated (cf. [15]). For such points, we fix the relative orientation of the orthonormal strain eigenvectors by letting

$$\xi_2 = \Omega \xi_1, \qquad \Omega = \begin{pmatrix} 0 & -1 \\ 1 & 0 \end{pmatrix}. \tag{6}$$

Motivated by the canonical examples of Section 2, we seek transport barriers at time t_0 as material lines that are local minimizers of the length functional

$$l_{t_0}^t(\gamma_0) := l(\gamma_t). \tag{7}$$

Unlike in classic calculus of variations problems, the end points of the extremal curves of $l_{t_0}^t$ are *a priori* unknown. Nevertheless, we can still write material lines C^1-close to the yet unknown extremum γ_0 in the form $r(s) + h(s)$, where

$$h\colon [s_1, s_2] \mapsto \mathbb{R}^2, \qquad h(s) \perp r'(s),$$

is a pointwise normal, smooth perturbation to γ_0.

The first variation of $l_{t_0}^t$ along a local extremum curve γ_0 is given by

$$\begin{aligned} \delta l_{t_0}^t(\gamma_0)\,[h] &= \lim_{\varepsilon \to 0} \frac{d}{d\varepsilon} l(\gamma_\varepsilon) \\ &= \sqrt{2} \lim_{\varepsilon \to 0} \frac{d}{d\varepsilon} \\ &\quad \times \int_{s_1}^{s_2} \sqrt{L(r(s) + \varepsilon h(s), r'(s) + \varepsilon h'(s))} ds, \end{aligned} \tag{8}$$

with the function L defined as

$$L(r, r') = \frac{1}{2} \left\langle r', C_{t_0}^t(r) r' \right\rangle. \tag{9}$$

Computing the variation (8), we obtain

$$\begin{aligned} \delta l_{t_0}^t(\gamma_0)\,[h] &= \sqrt{2} \left[\partial_{r'} \sqrt{L(r, r')} \cdot h \right]_{s_1}^{s_2} \\ &+ \sqrt{2} \int_{s_1}^{s_2} \left[\partial_r \sqrt{L(r, r')} - \frac{d}{ds} \partial_{r'} \sqrt{L(r, r')} \right] \cdot h ds. \end{aligned} \tag{10}$$

For $l_{t_0}^t$ to admit an extremum on a curve γ_0, we require its first variation to vanish on γ_0:

$$\delta l_{t_0}^t(\gamma_0) = 0. \tag{11}$$

3.2. Boundary conditions for the stretched length functional

We seek minimizers for the functional $l_{t_0}^t$ that satisfy a computable (strong) Euler–Lagrange equation under the broadest possible conditions. To achieve this, we must select the boundary points $a = r(s_1)$ and $b = r(s_2)$ of γ_0 in a way that makes the bracketed boundary term in (10) vanish. As we shall see below, there are two natural ways to do this.

3.2.1. Hyperbolic boundary conditions

In the classic treatment of variable-endpoint variational problems (see, e.g., [16]), one would cancel out the boundary term in (10) by selecting endpoints satisfying

$$\partial_{r'} \sqrt{L(r, r')}\Big|_{a,b} = 0. \tag{12}$$

This would allow for general normal perturbations $h(s_{1,2})$ to γ_0 at its endpoints.

Note, however, that in our case,

$$\partial_{r'} \sqrt{L(r, r')}\Big|_{a,b} = \frac{C_{t_0}^t(r) r'}{2\sqrt{L(r, r')}}\Bigg|_{a,b} \neq 0 \tag{13}$$

holds for any curve γ_0 with well-defined tangents $r'(a), r'(b) \neq 0$, because the Cauchy–Green strain tensor $C_{t_0}^t(r)$ is positive definite.[2]

[2] The nonexistence of endpoints satisfying (12) is, in fact, not surprising: no curve γ_0 can minimize the stretching functional $l_{t_0}^t$ under the completely general endpoint perturbations allowed by (12). Indeed, for a slightly shorter initial curve, $\bar{\gamma}_0 \subset \gamma_0$, obtained from tangential perturbations to γ_0 at its endpoints, the advected curve $F_{t_0}^t(\bar{\gamma}_0)$ will always remain strictly a subset of γ_t, given that $F_{t_0}^t$ is a diffeomorphism. As a result, we will necessarily have $l_{t_0}^t(\bar{\gamma}_0) < l_{t_0}^t(\gamma_0)$, and hence γ_0 cannot be a local minimizer for $l_{t_0}^t$.

For this reason, we divert from the classic treatment of variable-endpoint variational problems by requiring

$$h(s_{1,2}) \perp \partial_{r'}\sqrt{L(r(s_{1,2}), r'(s_{1,2}))}. \tag{14}$$

This boundary condition still ensures the cancellation of the boundary term in (10), and leads to the requirement

$$C_{t_0}^t\left(r(s_{1,2})\right) r'(s_{1,2}) \parallel r'(s_{1,2}),$$

i.e., $r'(s_{1,2})$ must be an eigenvector of the Cauchy–Green strain tensor. Since we are looking for a local minimum of $l_{t_0}^t$, we choose the relevant eigenvector to be $\xi_1(r'(s_{1,2}))$, the eigenvector corresponding to the smaller eigenvalue $\lambda_1(r(s_{1,2}))$ of $C_{t_0}^t\left(r(s_{1,2})\right)$. We therefore require

$$r(s_2) \neq r(s_1), \qquad r'(s_i) = \xi_1(r(s_i)), \quad i = 1, 2 \tag{15}$$

at the endpoints of γ_0.

This choice of the boundary conditions implies that, at least at its endpoints, the curve γ_0 exhibits the largest possible normal repulsion, as measured by the locally largest Lagrangian strain $\lambda_2(r(s_{1,2}))$. This is consistent with the strongest normal repulsion and attraction property of the stable and unstable manifolds in our first motivating example, as well as with the recently identified locally maximal repulsion property of hyperbolic Lagrangian Coherent Structures (LCSs) for general unsteady flows (see [11]). This prompts us to refer to the specialized variable-endpoint boundary conditions (15) as *hyperbolic boundary conditions*.

3.2.2. Shear boundary conditions

Here we seek to ensure the cancellation of the boundary terms in (10) in a way different from (15). The second way to ensure this cancellation is to simply require fixed-end boundary conditions. To eliminate any overlap between this class of boundary conditions and (15), we require

$$r(s_1) \neq r(s_2), \qquad r'(s_{1,2}) \nparallel \xi_1(r(s_{1,2})), \qquad h(s_{1,2}) = 0, \tag{16}$$

i.e., define the fixed-end boundary conditions for curves that do not already satisfy hyperbolic boundary conditions.

Note, however, that the fixed-end boundary conditions in (16) only exclude one tangential direction for the curve γ_0 at each of its endpoints. Therefore, (16) will typically lead to a minimizer between *any* two points a and b of the planar domain U (cf. our Remark 1 later on the Hopf–Rinow theorem). Clearly, the vast majority of these curves would lack any significance for the overall dynamics of system (1).

To make the boundary conditions (16) more specific, observe that out of all transport barriers, hyperbolic boundary conditions distinguish those whose endpoint-tangents align with directions of maximum compression. Keeping our second and third motivational examples (the shear jet and KAM curves) in mind, we now seek transport barriers that fall in the other extreme by maximizing an appropriately defined Lagrangian shear along their endpoint-tangents.

As we show in Appendix A, prescribing such tangents at the endpoints of γ_0 leads to the more specific boundary conditions

$$\begin{aligned} &h(s_{1,2}) = 0, \qquad r'(s_1) = \eta_\pm(r(s_1)), \\ &r'(s_2) = \eta_\pm(r(s_2)), \qquad r(s_1) \neq r(s_2), \end{aligned} \tag{17}$$

where the normalized Lagrangian *shear vector fields* $\eta_\pm(x)$ are defined as

$$\eta_\pm = \sqrt{\frac{\sqrt{\lambda_2}}{\sqrt{\lambda_1}+\sqrt{\lambda_2}}}\,\xi_1 \pm \sqrt{\frac{\sqrt{\lambda_1}}{\sqrt{\lambda_1}+\sqrt{\lambda_2}}}\,\xi_2, \tag{18}$$

with the plus (minus) sign referring to the direction of maximal positive (negative) shear in the frame of $[\xi_1, \xi_2]$. We refer to the fixed-endpoint boundary conditions (17) as *shear boundary conditions*.

We note that the shear vector field $\eta_\pm(x)$ is derived as the direction field that locally maximizes the Lagrangian shear $\sigma(x_0, e_0)$ introduced in Appendix A. As we show, this notion of material shear is different from the classic notion of shear strain used in continuum mechanics (cf. Appendix A.4).

4. Definitions and existence result for transport barriers

Based on the above discussion, we now formally define what we mean by a transport barrier, and state a result on the existence of such barriers.

Definition 1. A *transport barrier* of system (1) over the time interval $[t_0, t]$ is a material line γ_t, whose initial position γ_0 is a minimizer of the length functional $l_{t_0}^t$ under the boundary conditions (15) or (17).

Observe that our definition of a transport barrier has a finite time scale $T = t - t_0$ associated with it. We classify such finite-time transport barriers as follows:

Definition 2. A transport barrier γ_t is a *hyperbolic barrier* if γ_0 satisfies hyperbolic boundary conditions as defined in (15). A transport barrier γ_t is a *shear barrier* if γ_0 satisfies shear boundary conditions as defined in (17).

Using these definitions and the analysis of natural boundary conditions for transport barriers in Section 3.2, we obtain the following result.

Theorem 1. *Assume that γ_t is a transport barrier. Then*

(i) γ_0 is a geodesic on the Riemannian manifold (U, c), with the Riemannian metric c defined at each $x \in U$ as

$$c_x(u, v) = \left\langle u, C_{t_0}^t(x)v\right\rangle, \tag{19}$$

as long as $F_{t_0}^\tau(x) \in U$ holds for all times $\tau \in [t_0, t]$.

(ii) Let C_{lk} denote the (l, k) entry of the Cauchy–Green strain tensor $C_{t_0}^t$, and C^{il} denote the (i, l) entry of the inverse Cauchy–Green strain tensor $\left[C_{t_0}^t\right]^{-1}$. Then an appropriate parametrization $r(s) = \left(r^1(s), r^2(s)\right)$ of γ_0 satisfies the system of differential equations

$$\left(r^i\right)'' + \Gamma_{jk}^i \left(r^j\right)' \left(r^k\right)' = 0, \tag{20}$$

with summation implied over repeated indices, and with the Christoffel symbols Γ_{jk}^i defined as

$$\Gamma_{jk}^i = \frac{1}{2}C^{il}\left(C_{lj,k} + C_{lk,j} - C_{jk,l}\right), \qquad C^{il}C_{lk} = \delta_k^i. \tag{21}$$

(iii) With the generalized momentum p defined as

$p = \partial_{r'}L = C_{t_0}^t(r)r'$,

the parametrization $r(s)$ of γ_0 also satisfies the first-order system of differential equations

$$\begin{aligned} r' &= \left[C_{t_0}^t(r)\right]^{-1} p, \\ p' &= -\frac{1}{2}\partial_r \left\langle p, \left[C_{t_0}^t(r)\right]^{-1} p\right\rangle, \end{aligned} \tag{22}$$

which is a canonical Hamiltonian system with Hamiltonian

$$H(r, p) = \frac{1}{2}\left\langle p, \left[C_{t_0}^t(r)\right]^{-1} p\right\rangle. \tag{23}$$

Proof. See Appendix B. □

Remark 1. Since U is a compact subset of $\mathbb{R}^2$, the Hopf–Rinow theorem (cf. [17]) guarantees that any two points of U are connected by a geodesic under the Cauchy–Green metric c. This fact underlines the role of hyperbolic and shear boundary conditions in distinguishing transport barriers from ordinary geodesics. Indeed, the latter can be found between *any* two points of the physical domain U.

Remark 2. In differential geometric terms, the Cauchy–Green metric is just the pullback metric $c = \left(F_{t_0}^t\right)^* e$, with e denoting the standard two-dimensional Euclidean metric. As a consequence, geodesics of c are pre-images of straight lines (i.e., the geodesics of e) under the flow map $F_t^{t_0}$. As such, all Cauchy–Green geodesics can be written in the explicit, parametrized form

$$r(s; r_0, r_0') = F_t^{t_0}\left(F_{t_0}^t(r_0) + sDF_{t_0}^t(r_0)r_0'\right). \tag{24}$$

Such a geodesic can be launched from any point r_0 along any initial unit tangent r_0'. Out of this abundance of curves, we will focus on the ones with the most tangible impact on transport.

Remark 3. The Hamiltonian (23) can also be viewed as that of a freely moving particle on the space $F_{t_0}^t(U)$, with the preimage r of the particle under the flow map used as a generalized coordinate, and with the generalized momentum vector p canonically conjugate to r. For details, see Appendix C.

5. Homogeneous (idealized) transport barriers

A transport barrier, as defined in Definition 1, will have the most prominent effect on nearby trajectories if all its subsets behave in the same fashion relative to nearby trajectories. We now define special transport barriers with this property.

Definition 3. We call a transport barrier γ_t over $[t_0, t]$ *homogeneous* if any material line $\bar{\gamma}_t \subset \gamma_t$ is also a transport barrier of system (1) over the time interval $[t_0, t]$ in the sense of Definition 1, with $\bar{\gamma}_0$ satisfying the same type of boundary conditions as γ_0 does.

In addition to solving the two-dimensional set of second-order Euler–Lagrange equations, homogeneous transport barriers solve simpler first-order differential equations.

Proposition 1. *Let γ_t be a homogeneous transport barrier over the time interval $[t_0, t]$. Assume that $\gamma_0 \subset U_0$, where $U_0 \subset U$ is an open set in which the unit strain eigenvector fields, $\xi_1(x)$ and $\xi_2(x)$, of the Cauchy–Green strain tensor field $C_{t_0}^t(x)$ are smooth.*

(i) *If γ_t is a hyperbolic transport barrier, then γ_0 is a* strainline *, i.e., a trajectory of the differential equation*

$$r' = \xi_1(r). \tag{25}$$

(ii) *If γ_t is a shear barrier, then γ_0 is a* shearline *, i.e., a trajectory of the differential equation*

$$r' = \eta_\pm(r), \tag{26}$$

with either the $+$ or the $-$ sign chosen in the definition (18) of the shear vector field $\eta_\pm$.

Proof. Since γ_t is a homogeneous transport barrier, any $\bar{\gamma}_t \subset \gamma_t$ must be a transport barrier of the same type. Now any point $r \in \gamma_0$ is the endpoint of some $\bar{\gamma}_0 \subset \gamma_0$, therefore Eqs. (15) and (17), as well as the smoothness of the $\xi_i(x)$ fields imply the statements of the proposition. □

Shown in Fig. 4, homogeneous transport barriers are ideally the most observable inhibitors of transport, with all their subsets consistently behaving as hyperbolic or shear barriers. Such geodesics are highly constrained, however, and hence may not exist in a generic unsteady flow over a given time scale. In Appendix D, we review two classes of unsteady flows with homogeneous transport barriers: non-autonomous linear systems and non-autonomous parallel shear flows.

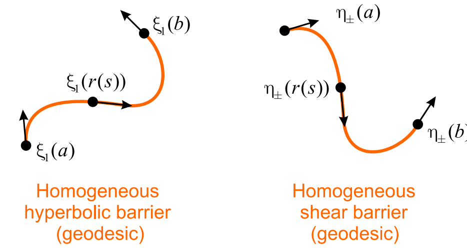

Fig. 4. Homogeneous transport barriers are idealized transport barriers that coincide with locally least-stretching geodesics, satisfying the same hyperbolic or shear boundary conditions at all their points. *Lower panel*: Near-homogeneous transport barriers satisfy hyperbolic or shear boundary conditions at each of their points, and are shadowed closely (in the C^2 metric) by locally least-stretching Cauchy–Green geodesics.

6. Near-homogeneous transport barriers

The examples of Appendix D underline the significance of homogeneous transport barriers in idealized flows. As noted above, however, typical flows may not admit barriers that are exactly homogeneous. Motivated by these observations, we seek near-homogeneous transport barriers as special material lines that, at the initial time t_0, satisfy hyperbolic or shear boundary conditions at each of their points at time t_0, *and* are closely shadowed by least-stretching Cauchy–Green geodesics. Such material lines are necessarily strainlines or shearlines, respectively, by Proposition 1, but are not necessarily exact geodesics. Their closeness to least-stretching geodesics distinguishes them, because least-stretching geodesics – as locally the most stretching images of straight material lines under the inverse flow map – are the most capable of wrapping around transport barriers in backward time.

6.1. Detection of near-homogeneous barriers

Let a smooth curve $\gamma_{t_0}(s) \subset U$ be a candidate for a near-homogeneous transport barrier at time t_0. Consider a point $p = \gamma_{t_0}(s_p)$, and let the curve $r(s)$ denote the *least-stretching geodesic* at p under the Cauchy–Green metric c, i.e., the geodesic starting from p in the least-stretching direction with a unit tangent vector:

$$r(s_p) = p, \qquad r'(s_p) = \xi_1(r(s_p)).$$

Definition 4. The *geodesic deviation* $d_g(p)$ of the transport barrier candidate $\gamma_{t_0}(s)$ at the point p is defined as the local C^2 distance of $\gamma_{t_0}(s)$ from $r(s)$ at the point p:

$$d_g(p) = \left|1 - \frac{\langle \gamma_{t_0}'(s_p), r'(s_p)\rangle}{|\gamma_{t_0}'(s_p)|\,|r'(s_p)|}\right| + \left|\frac{\det(\gamma_{t_0}'(s_p), \gamma_{t_0}''(s_p))}{|\gamma_{t_0}'(s_p)|^3} - \frac{\det(r'(s_p), r''(s_p))}{|r'(s_p)|^3}\right|. \tag{27}$$

Note that $d_g(p)$ deems the curve $\gamma_{t_0}(s)$ and the least-stretching geodesic $r(s)$ close at p if both their tangents and their curvatures are close. Also note that *if* the curve $\gamma_{t_0}(s)$ is a strainline, then the first term in the definition (27) vanishes, and hence $d_g(p)$ becomes analogous to the classic expression for geodesic curvature.[3]

[3] Note that the classic notion of geodesic curvature measures how close curves on two-dimensional surfaces in $\mathbb{R}^3$ are to geodesics. Instead of embedding our inherently two-dimensional problem in $\mathbb{R}^3$ and developing further machinery to apply related classic results, we can define an equivalent notion of geodesic curvature for curves in our flow domain U. If we were to embed U as a two-

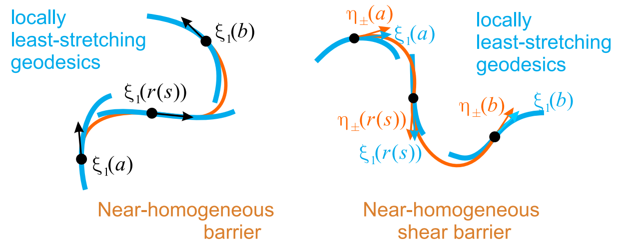

Fig. 5. Near-homogeneous transport barriers at time t_0 satisfy hyperbolic or shear boundary conditions at each of their points, and are shadowed closely (in the C^2 metric) by locally least-stretching Cauchy–Green geodesics.

Assuming that $|\gamma_{t_0}(s_p)| = 1$ and recalling $|r'(s_p)| = |\xi_1(r(s_p))| = 1$, substitution of the tangent vector $r'(s_p) = \xi_1(r(s_p))$ into the geodesic equations (20) enables us to rewrite (27) as

$$d_g(p) = \left|1 - \langle \gamma'_{t_0}(s_p), \xi_1(p)\rangle\right| + \left|\langle \gamma''_{t_0}(s_p), \Omega\gamma'_{t_0}(s_p)\rangle - \langle G(p, \xi_1(p)), \xi_2(p)\rangle\right| \tag{28}$$

where Ω is the skew-symmetric matrix introduced in (6), and the vector-valued function G is defined as

$$G(r, u) = -\begin{pmatrix} \Gamma^1_{jk}(r)u^j u^k \\ \Gamma^2_{jk}(r)u^j u^k \end{pmatrix}, \tag{29}$$

with summation implied over repeated indices. We now formally define when we consider the evolving material line $\gamma_t = F^t_{t_0}(\gamma_{t_0})$ a near-homogeneous transport barrier over the time interval $[t_0, t]$.

Definition 5. For some small constant $\epsilon \geq 0$, a compact and connected material line γ_t is a *near-homogeneous barrier of order* ϵ over the time interval $[t_0, t_0 + T]$ if for any point $p \in \gamma_{t_0}$, the geodesic deviation (27) satisfies

$$d_g(p) \leq \epsilon,$$

with d_g computed using the invariants of the Cauchy–Green strain tensor $C^{t_0+T}_{t_0}$.

A near-homogeneous barrier γ_t will again be classified as a hyperbolic or a shear barrier if γ_{t_0} is a strainline or a shearline, respectively. Note that a near-homogeneous transport barrier is fully Lagrangian (invariant) under the flow, and is guaranteed to be shadowed by locally least-stretching geodesics (see Fig. 5).

Below we derive explicit formulae for the geodesic deviation of two important barrier candidates, strainlines and shearlines. This will enable us to identify trajectory segments of the strain and shear differential equations that qualify as near-homogeneous transport barriers of a given order ϵ. In stating the results, we will use the quantities

$$\kappa_2 = \langle \nabla\xi_2\xi_2, \xi_1\rangle, \qquad \kappa_1 = \langle \nabla\xi_1\xi_1, \xi_2\rangle, \tag{30}$$

where κ_i measures the Euclidean curvature of a trajectory of the ξ_i vector field with respect to the trajectory's unit normal ξ_j, with $i \neq j$. We also use the notation

$$\alpha := \sqrt{\frac{\sqrt{\lambda_2}}{\sqrt{\lambda_1} + \sqrt{\lambda_2}}}, \qquad \beta := \sqrt{\frac{\sqrt{\lambda_1}}{\sqrt{\lambda_1} + \sqrt{\lambda_2}}},$$

for the coefficients of ξ_1 and $\pm\xi_2$, respectively, in the expression (18).

Theorem 2 (*Geodesic Deviation of Strainlines and Shearlines*).

(i) *At any point p with $\lambda_1 \neq \lambda_2$, the geodesic deviation of the strainline through p is given by*

$$d_g^{\xi_1} = \frac{1}{\lambda_2}\left|\lambda_1\kappa_1 - \frac{1}{2}\langle \nabla\lambda_1, \xi_2\rangle\right|. \tag{31}$$

For incompressible flows ($\nabla \cdot v = 0$), formula (31) can also be written as

$$d_g^{\xi_1} = \frac{1}{\lambda_2^2}\left|\kappa_1 + \frac{1}{2\lambda_2}\langle \nabla\lambda_2, \xi_2\rangle\right|. \tag{32}$$

(ii) *At any point p with $\lambda_1 \neq \lambda_2$, the geodesic deviation of the shearline through p is given by*

$$d_g^{\eta\pm} = |1-\alpha| + \left|\mp\frac{1}{\beta}\langle \nabla\alpha, \eta_\pm\rangle + \alpha\kappa_1 \mp \beta\kappa_2 + \left(\frac{\lambda_1}{\lambda_2} - 1\right)\kappa_1 - \frac{1}{2\lambda_2}\langle \nabla\lambda_1, \xi_2\rangle\right|. \tag{33}$$

For incompressible flows ($\nabla \cdot v = 0$), formula (33) can also be written as

$$d_g^{\eta\pm} = \frac{\sqrt{1+\lambda_2} - \sqrt{\lambda_2}}{\sqrt{1+\lambda_2}} + \left|\frac{\langle \nabla\lambda_2, \xi_1\rangle}{2\lambda_2\sqrt{1+\lambda_2}} \mp \frac{\langle \nabla\lambda_2, \xi_2\rangle\left(\sqrt{1+\lambda_2}^3 - \sqrt{\lambda_2}^5\right)}{2\lambda_2^3\sqrt{1+\lambda_2}^3} \mp \frac{\kappa_1\left[\sqrt{\lambda_2}^5 + (1-\lambda_2^2)\sqrt{1+\lambda_2}\right]}{\lambda_2^2\sqrt{1+\lambda_2}} + \frac{\kappa_2}{\sqrt{1+\lambda_2}}\right|. \tag{34}$$

(iii) *At any point p with $\lambda_1 \neq \lambda_2$, the geodesic deviation of a general near-homogeneous transport barrier candidate $\gamma_{t_0}(s)$ through p is given by*

$$d_g = \left|1 - (\gamma_0^i)'\xi_1^i/|\gamma_0'|\right| + \left|\Omega_{ij}\left[(\gamma_0^i)''\left(\gamma_0^j\right)'/|\gamma_0'|^{3/2} - F^{i,jl}F_{j,k}F_{l,m}\left(\xi_1^j\right)'\left(\xi_1^k\right)'\left(\xi_1^m\right)'\right]\right|, \tag{35}$$

with summation implied over repeated indices, and with F_i and F^i referring to the ith coordinate function of the flow map $F^t_{t_0}$ and its inverse, $F^{t_0}_t$, respectively.

Proof. See Appendix E. □

For any fixed bound $\epsilon > 0$, Theorem 2 provides a quantitative tool to assess whether a given strainline or shearline is a near-homogeneous transport barrier of order ϵ. Further assistance in classifying transport barriers is provided below.

6.2. Incompressible near-homogeneous barriers: Elliptic, parabolic and hyperbolic barriers

Here we discuss a general classification of near-homogeneous transport barriers in two-dimensional incompressible (area-preserving) dynamical systems. We start with a result that underlines the significance of closed shear barriers.

Proposition 2. *Assume that the dynamical system (1) is incompressible ($\nabla \cdot v = 0$). Let $\gamma_{t_0} \subset U$ denote a compact shearline of the shear-vector field $\eta_\pm(r)$, computed from the Cauchy–Green strain tensor field $C^{t_0+T}_{t_0}$. Then the arclength of γ_{t_0} is preserved under the flow map $F^{t_0+T}_{t_0}$.*

dimensional surface in $\mathbb{R}^3$ through the map $x \mapsto (F^t_{t_0}(x), 0)$, the classic definition of geodesic curvature would turn out to be a scalar multiple of the one given here, with the scalar being $\sqrt{\det C^t_{t_0}(r)}$. This can be concluded by applying Beltrami's formula for the geodesic curvature in this three-dimensional context (see, e.g., [18]).

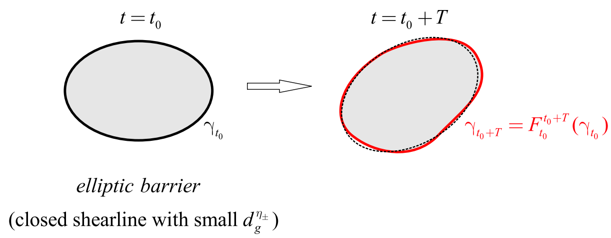

Fig. 6. Schematic of an elliptic transport barrier. A closed shearline γ_{t_0}, computed from flow data over $[t_0, t_0 + T]$, plays the role of a generalized KAM curve. Broken line indicates a hypothetical translated and rotated position of γ_{t_0} for reference. The advected material line γ_{t_0+T} has the same arclength, and encloses the same area as γ_{t_0} does.

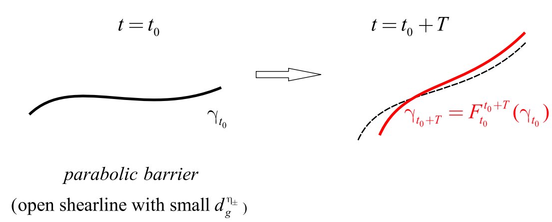

Fig. 7. Schematic of a parabolic transport barrier. An open shearline γ_{t_0}, computed from flow data over $[t_0, t_0 + T]$, plays the role of a filament in a generalized shear jet. The broken line indicates a hypothetical translated and rotated position of γ_{t_0} for reference. The advected material line γ_{t_0+T} has the same arclength as γ_{t_0} does.

Proof. See Appendix F. □

Since the mapping $F_{t_0}^{t_0+T}$ is area-preserving in an incompressible flow, Proposition 2 implies that closed shearlines in incompressible flows preserve both their arclength and the area they enclose. Since typical closed material lines will increase their arclength due to stretching, folding and shear in the flow, those preserving their arclength clearly have special significance.

Namely, while the flow map $F_{t_0}^{t_0+T}$ may translate and rotate closed shearlines substantially, it can only transport them with modest deformation, because of their arclength and enclosed area must be preserved between the times t_0 and $t_0 + T$. Note that it is such a simultaneous preservation of arclength and enclosed area makes classic KAM curves distinguished inhibitors of phase space transport. In particular, they are boundaries of open sets that show no visible mixing with their exteriors.

By Proposition 2, therefore, closed shearlines with small $\langle d_g \rangle$ values can be considered *elliptic barriers (generalized KAM curves)* in incompressible, finite-time, non-autonomous dynamical systems on the plane (cf. Fig. 6).

The preservation of arclength established in Proposition 2 is equally applicable to open shearlines. Such shearlines can be best thought of as frame-independent generalizations of the non-stretching streamlines forming the steady shear jet shown in Fig. 2. Motivated by this analogy, we refer to groups of open shearlines with small $\langle d_g \rangle$ values as *parabolic barriers (generalized shear jets)*. We sketch the related geometry in Fig. 7.

Finally, strainlines obtained from the eigenvector field of the Cauchy–Green strain tensor field $C_{t_0}^{t_0+T}(x_0)$ will show contraction in an incompressible flow, given that $\lambda_1(x_0) < 1$ will typically hold in such flows. Accordingly, for $T > 0$, we refer to strainline segments with pointwise small d_g values as *forward-hyperbolic barriers* (*generalized stable manifolds*) at time t_0. Similarly, for $T < 0$, we refer to strainlines segments with small d_g values as *backward-hyperbolic barriers* (*generalized unstable manifolds*) at time t_0. We sketch the related geometry in Fig. 8.

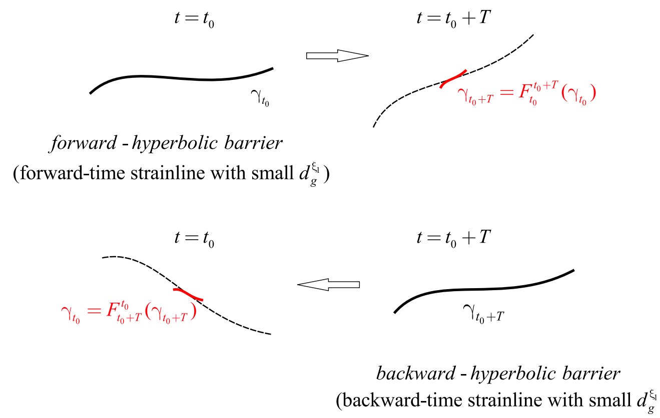

Fig. 8. Schematic of forward- and backward-hyperbolic transport barriers. Strainlines γ_{t_0} and γ_{t_0+T}, computed from flow data over $[t_0, t_0 + T]$ and $[t_0 + T, t_0]$, play the role of generalized stable and unstable manifolds, respectively. Broken lines indicate hypothetical translated and rotated positions of γ_{t_0} and γ_{t_0+T} for reference. The arclength of γ_{t_0} and γ_{t_0+T} shrinks exponentially under forward-time and backward-time advection, respectively, by the flow map.

7. Computation of transport barriers

7.1. Numerical algorithm

Proposition 1 and Theorem 2 establish the mathematical foundation for the computation of near-homogeneous transport barriers from finite-time flow data. The main steps in the algorithm are the following:

I. Select small positive parameters ϵ_{ξ_1} and $\epsilon_{\eta_\pm}$ as admissible upper bounds for the geodesic deviation of near-homogeneous transport barriers.
II. For a given finite time interval $[t_0, t_0 + T]$ of interest, compute the flow map $F_{t_0}^{t_0+T}$ over initial conditions x_0 taken from a grid $\mathcal{G}_0$.
III. Calculate the Cauchy–Green strain tensor field $C_{t_0}^{t_0+T}(x_0)$, as well as its eigenvalue fields $\lambda_i(x_0)$ and eigenvector fields $\xi_i(x_0)$, over $\mathcal{G}_0$.
IV. Calculate strainlines and shearlines by solving the ODEs (25) and (26) numerically, starting from each point $x_0 \in \mathcal{G}_0$. (Interpolate the shear and strain vector fields between grid points.)
V. Locate the set $\Sigma(t_0, t_0 + T, \epsilon_{\xi_1})$ of strainline segments on which the pointwise geodesic deviation $d_g^{\xi_1}$ is no larger than ϵ_{ξ_1}. Then identify *forward-hyperbolic barriers* as strainline segments γ_{t_0} whose relative stretching

$$q(\gamma_{t_0}) = l(\gamma_{t_0+T})/l(\gamma_{t_0}) \tag{36}$$

is locally minimal among neighboring strainline segments in $\Sigma(t_0, t_0 + T, \epsilon_{\xi_1})$ (cf. Section 7.4).
VI. Identify *parabolic barriers* of order $\epsilon_{\eta_\pm}$ at time t_0 as open shearline segments on which the average geodesic deviation $\langle d_g^{\eta_\pm} \rangle$ is no larger than $\epsilon_{\eta_\pm}$ (cf. Section 7.4).
VII. Identify *elliptic barriers* of order $\epsilon_{\eta_\pm}$ at time t_0 as closed shearlines on which the average geodesic deviation $\langle d_g^{\eta_\pm} \rangle$ is no larger than $\epsilon_{\eta_\pm}$ (cf. Section 7.4).
VIII. To obtain hyperbolic, parabolic and elliptic barriers at an arbitrary time $t \in [t_0, t_0 + T]$, advect the barriers identified at time t_0 as material lines using the flow map $F_{t_0}^{t}$.
IX. To obtain *backward-hyperbolic barriers* at time t_0, repeat steps I–VIII, using the inverse flow map $F_{t_0}^{t_0-T}$. [4]

[4] This step identifies transport barriers that are locally least-stretching in backward time over the time interval $[t_0 - T, t_0]$. The properties of these material

Below we summarize the main numerical challenges involved in performing steps I–IX.

7.2. Computing strain eigenvalues and eigenvectors

A direct computation of the λ_1 and ξ_1 fields is usually less accurate than that of λ_2 and ξ_2, because of the attracting nature of the strongest eigenvector of $C_{t_0}^{t_0+T}$. For this reason, computing λ_1 in terms of λ_2 in (31) and (33) is preferable. If the flow is incompressible, this is simply achieved using the relation $\lambda_1\lambda_2 = 1$. In the compressible case, we recall from Liouville's theorem [19] that for a general compressible flow,

$$\det DF_{t_0}^t(x_0) = \exp\left[\int_{t_0}^{t_0+T} \operatorname{div} v(F_{t_0}^t(x_0), t)dt\right]. \tag{37}$$

Noting that $\lambda_1 = \det C_{t_0}^{t_0+T}/\lambda_2 = \left[\det DF_{t_0}^t\right]^2/\lambda_2$, we obtain the expression

$$\lambda_1(x_0) = \frac{1}{\lambda_2(x_0)} \exp\left[2\int_{t_0}^{t_0+T} \operatorname{div} v(F_{t_0}^t(x_0), t)dt\right], \tag{38}$$

to be used in the numerical computation of the general formulae (31) and (33). In general, the weaker strain eigenvector is best computed from (6) as $\xi_1 = -\Omega\xi_2$.

Computing the λ_2 and ξ_2 fields accurately typically requires the use of an auxiliary grid, i.e., four additional grid points around each primary grid point in $\mathcal{G}_0$. The auxiliary grid points can be selected arbitrarily close to the primary grid points, thereby increasing the precision of finite-differencing involved in computing the entries of $C_{t_0}^{t_0+T}$ (see [20] for more detail).

7.3. Computing strainlines and shearlines

Away from degenerate points with $\lambda_1 = \lambda_2$, the eigenspaces of the Cauchy–Green strain tensor field $C_{t_0}^t(r)$ vary smoothly as a function of the location r. Despite this smooth variation is space, the eigenspace field is typically not an orientable vector bundle, and hence the normalized eigenvector fields $\xi_1(r)$ and $\xi_2(r)$ admit orientational discontinuities. As a result, even though strainlines and shearlines are well-defined smooth curves away from repeated strain eigenvalues, the computation of these lines as trajectories of the discontinuous ODEs (25) and (26) requires special care.

Strainlines also arise – as pointwise most repelling material lines – in the computation of hyperbolic Lagrangian Coherent Structures (LCSs). As discussed by Farazmand and Haller [20] in that context, a scaling suggested in [21] for general tensor lines can be applied to facilitate the integration of (25). Specifically, degenerate points are transformed into fixed points, and orientational discontinuities are eliminated along trajectories in the scaled strain ODE

$$r'(s) = \operatorname{sign}\left\langle \xi_1(r(s)), r'(s-\Delta)\right\rangle z(r(s))\xi_1(r(s)), \tag{39}$$

with $\Delta > 0$ denoting the numerical stepsize, and with the scalar field $z(r)$ defined as

$$z(r) := \left(\frac{\lambda_2(r) - \lambda_1(r)}{\lambda_1(r) + \lambda_2(r)}\right)^2. \tag{40}$$

Similarly, shearlines are obtained as smooth, nontrivial trajectories of the scaled shear ODEs

$$r'(s) = \operatorname{sign}\left\langle \eta_\pm(r(s)), r'(s-\Delta)\right\rangle z(r(s))\eta_\pm(r(s)). \tag{41}$$

Note that the numerical schemes used in (39) and (41) can be viewed as discretizations of delay-differential equations, and hence can produce trajectories that are significantly more complex than solutions of autonomous planar differential equations. Indeed, some well-known transport barriers, such as homoclinic tangles and strange attractors, show self-accumulation that could not be captured by trajectories of smooth planar ODEs.

7.4. Extracting transport barriers from strainlines

We seek hyperbolic transport barriers as material lines that are C^2-close to locally least-stretching Cauchy–Green geodesics satisfying hyperbolic boundary conditions (cf. Section 6.2). Introduced in (15), hyperbolic boundary conditions ensure that the underlying geodesic stays locally least-stretching even under normal perturbations to its endpoints. If the geodesic is homogeneous (cf. Definition 3), it satisfies hyperbolic boundary conditions at all its points, and hence remains locally least stretching among all C^1 close material curves. This uniqueness under all normal perturbations is a property we want to enforce for near-homogeneous barriers in our computations.

To this end, recall from Step V in Section 7.1 that $\Sigma(t_{0,}t_0+T, \epsilon_{\xi_1})$ is defined as the set of strainline segments along which $d_g^{\xi_1} \le \epsilon_{\xi_1}$ holds pointwise. The error bar $\epsilon_{\xi_1} > 0$ is the maximum admissible error we fix for the pointwise C^2 distance of a detected transport barrier from a locally least-stretching Cauchy–Green geodesic. In exceedingly short data sets, none of the strainlines may meet this admissible error bar. In general, however, the longer flow data we have, the more pronounced the barriers become, and the smaller ϵ_{ξ_1} can be selected.

We seek strainline segments in $\Sigma(t_{0,}t_0 + T, \epsilon_{\xi_1})$ that are locally the least stretching among their immediate neighbors.[5] The computation of the invariants of $C_{t_0}^{t_0+T}$, and hence of the direction field $\xi_1(x_0)$, will be the noisiest precisely near such strainlines. Even if $\xi_1(x_0)$ were accurately computed, its trajectories will generally show the highest sensitivity with respect to initial conditions near least-stretching strainlines. In our experience, these numerical effects tend to create oscillations in the relative stretching function (36), leading to additional spurious local minima in the search for the locally least stretching strainline segment.

To eliminate such spurious minima, we first compute the relative stretching function on each connected strainline segment intersecting a reference line L_0 of initial conditions. Restricted to L_0, we have $\Delta(x_0) := q(\gamma_{t_0})$, a function over a one-dimensional domain parametrized by $x_0 \in L_0 \cap \gamma_{t_0}$. The intersection set $L_0 \cap \gamma_{t_0}$ may contain several points, but at each of those points, the relative stretching function $\Delta(x_0)$ takes the same value $q(\gamma_{t_0})$ by definition.

If $M(L_0)$ denotes the set of strict local minima of $\Delta(x_0)$ along L_0, then we define the set $S(L_0)$ as the set of *super minima* of $\Delta(x_0)$ along L_0, i.e., the set of (not necessarily strict) local minima of $\Delta(x_0)$ within the discrete set $M(L_0)$. This two-pass minimization of the relative stretching along L_0 aims to eliminate spurious relative minima arising from numerical noise and sensitive dependence, as

lines over the time interval $[t_0, t_0+T]$ considered in steps I–IX, is a priori unknown. Alternatively, one may apply the geodesic theory to the inverse flow map $F_{t_0+T}^{t_0}$ to obtain barriers at $t = t_0 + T$ that are locally least-stretching over the original time interval $[t_0, t_0 + T]$ in backward time. Advecting these barriers back to their $t = t_0$ position under $F_{t_0+T}^{t_0}$, however, will typically yield very short material lines at time t_0 due to the high rate of contraction along the identified barriers in backward time.

[5] This numerical step enforces our original principle to find locally least-stretching material lines. The computation of strainlines reduces this search to a one-parameter family of candidates (strainline segments) that are least-stretching under perturbations to their tangent spaces, but not necessarily under parallel translations, given that strainlines are typically are not exact Cauchy–Green geodesics. Finding then the locally least-stretching strainlines completes the search for least-stretching material lines within the strainline family.

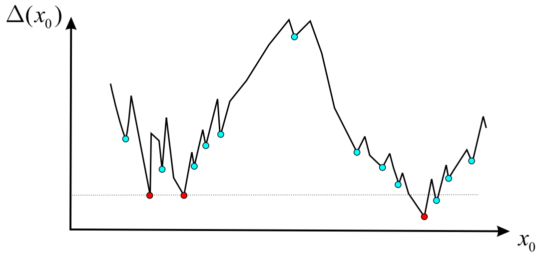

Fig. 9. The construction of super minima (red dots) from simple local minima (blue dots), to be used in locating intersections of locally minimally stretching strainlines with a line L_0 of initial conditions, parametrized by the coordinate x_0. (For interpretation of the references to colour in this figure legend, the reader is referred to the web version of this article.)

illustrated in Fig. 9. In an actual numerical implementation, $M(L_0)$ will already be a discrete set, formed by a select number of initial conditions from which strainlines are launched. The first pass in minimizing $\Delta(x_0)$ only leads to a meaningful $M(L_0)$ if the strainline initial conditions along L_0 are chosen dense enough.

7.5. *Extracting transport barriers from shearlines*

Unlike hyperbolic boundary conditions, shear boundary conditions do not ensure a locally minimal stretching property for Cauchy–Green geodesics under perturbations to their endpoints. Indeed, as we have seen in our two canonical examples of shear barriers (KAM curves and filaments of shear jets), these material lines ought to be least-stretching only under perturbations that keep their endpoints fixed.

Accordingly, near-homogeneous shear barriers will generally not be the locally least-stretching among *all* nearby shearlines. Instead, they will be pointwise least-stretching with respect to perturbations to their tangents. This property allows a whole family of shear barriers to co-exist, the same way KAM curves and shear jet filaments form near-parallel material line families.

To find the most prominent shear barriers, therefore, we require members of a shearline family to be C^2-close *on average* to a family of locally least-stretching Cauchy–Green geodesics. Specifically, a compact and connected shearline segment γ_{t_0} is identified as a shear barrier if

$$\langle d_g\rangle(\gamma_{t_0}) := \frac{\int_{\gamma_{t_0}} d_g(r(s))\,|r'(s)|\,ds}{\int_{\gamma_{t_0}} |r'(s)|\,ds} \leq \epsilon_{\eta\pm} \tag{42}$$

with d_g computed using the invariants of the Cauchy–Green strain tensor $C_{t_0}^{t_0+T}$.

The small averaged geodesic deviation requirement (42) turns out to be highly effective in the computational detection of elliptic barriers. In our numerical experiments, we have found that $\epsilon_{\eta\pm}$ values of the order of 10^{-2} yield barriers that are practically indistinguishable from KAM curves (cf. Section 8).

7.6. *The length of the time interval used in barrier detection*

Beyond aiding the detection of transport barriers, geodesic deviation provides a way to optimize time integration for Lagrangian structure extraction. In light of the explicit solutions for geodesics obtained in formula (24), small values of geodesic deviation on a transport barrier candidate mean that straight lines advected in backward time stretch out and wrap tightly around this candidate material line. In forward time, this implies that prominent shearing or repelling action can be observed for the barrier over the forward-time interval over which the geodesic deviation was computed.

In particular, a hyperbolic barrier can be considered converged from a computation over the interval $[t_0, t_0+T]$ if its *pointwise* geodesic deviation is below a prescribed error bar. In our numerical studies, $d_g^{\xi_1} \leq 10^{-3}$ has yielded excellent agreement with known stable and unstable manifolds. Similarly, parabolic and elliptic barriers can be considered converged from a computation over $[t_0, t_0+T]$ if their *averaged* geodesic deviation is below a prescribed error bar. In our numerical studies, $\langle d_g^{\eta\pm}\rangle \leq 0.2$ has yielded elliptic barriers that were indistinguishable from known KAM tori. Remarkably, these converged barriers were obtained for T values significantly shorter than those needed to establish the same barriers with the same resolution from the direct iteration of Poincare maps (cf. Section 8).[6]

8. Example 1: Transport barriers in a two-dimensional chaotic advection mapping

In our first example, we verify that the geodesic transport theory developed here captures the most important transport barriers in a discrete dynamical system where those barriers can also be indirectly observed by simply iterating initial conditions under a two-dimensional mapping.

Pierrehumbert [23] proposed a smooth area-preserving map of the 2-torus $\mathbb{T}^2 := [-1/2, 1/2] \times [0, 1]$ to itself[7]:

$$P : \begin{pmatrix} x \\ y \end{pmatrix} \mapsto \begin{pmatrix} x + a\sin 2\pi y \\ y + a\sin[2\pi\,(x + a\sin 2\pi y)] \end{pmatrix}. \tag{43}$$

Physically, (43) models an incompressible time-periodic flow resulting from the superposition of two planar waves, one propagating in the x direction and the other in the y direction. The map (43) has four fixed points on the torus $\mathbb{T}^2$: two centers at $(-1/2, 0)$ and $(0, 1/2)$, respectively, and two saddles at $(-1/2, 1/2)$ and $(0, 0)$, respectively. The system is non-integrable for any $a > 0$, with the stable and unstable manifolds of the saddles forming heteroclinic tangles. For moderate values of a, the ensuing stochastic band is thin and surrounds KAM tori encircling the centers.

Fixing the parameter value $a = 0.2$, we explore below what part of these structures can be reconstructed accurately as transport barriers using a few iterations of the map. Note that the dynamical system (43) is not defined in terms of a velocity field, as assumed in (1), but directly through the discrete flow map $F_0^n := P^n$. Evaluating this map however, at any of the discrete time values $t = n \in \mathbb{Z}$ is sufficient for the application of the geodesic transport theory developed in this paper.

For reference, Fig. 10 shows a few representative hyperbolic and elliptic transport barriers obtained by iterating select initial conditions under P. Note that precise knowledge of the hyperbolic fixed points of P is essential in constructing the shown pieces of stable and unstable manifolds, which required $n = 14$ iterations. Also note the large number of iterations ($n = 10^4$) required for the visualization of primary and secondary KAM tori as continuous-looking curves.

Fig. 11 shows forward-hyperbolic barriers reconstructed from the numerical procedure outlined in Section 7.4. To resolve the details of the tangle, a numerical grid of 2000×2000 was used. Note the exact correspondence between the directly computed stable manifolds in Fig. 10 (obtained from $n = 14$ iteration) and

[6] Use of special algorithms for twist maps do accelerate the computation of KAM curves relative to a direct visualization through iterated Poincare maps (see, e.g., [22] for a review). The point here is that KAM curves emerge as geodesic transport barriers automatically, without the use of the symplectic structure or initial estimates for closed invariant curves. This spontaneous emergence enables the exploration of elliptic barriers in non-symplectic maps and, more importantly, in finite-time dynamical systems with general time dependence.

[7] For ease of working with planar coordinates, we now switch to the notation (x, y) from (x^1, x^2), which was used in earlier sections.

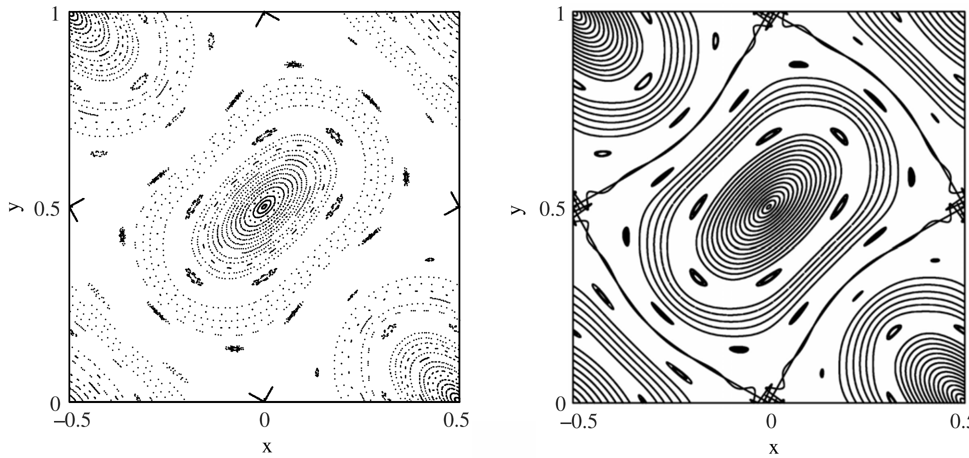

Fig. 10. Select transport barriers obtained from the iteration of the advection map P with $a = 0.2$. Left panel: Stable and unstable manifolds obtained from $n = 9$ forward and backward iterations of a small circle of radius 10^{-6}, centered at the known hyperbolic fixed points of P. The KAM tori are obtained from $n = 100$ iterations of select initial conditions. Right panel: Same as on the left, but using $n = 14$ iterations for the stable and unstable manifolds, and $n = 10^4$ iterations for the KAM tori.

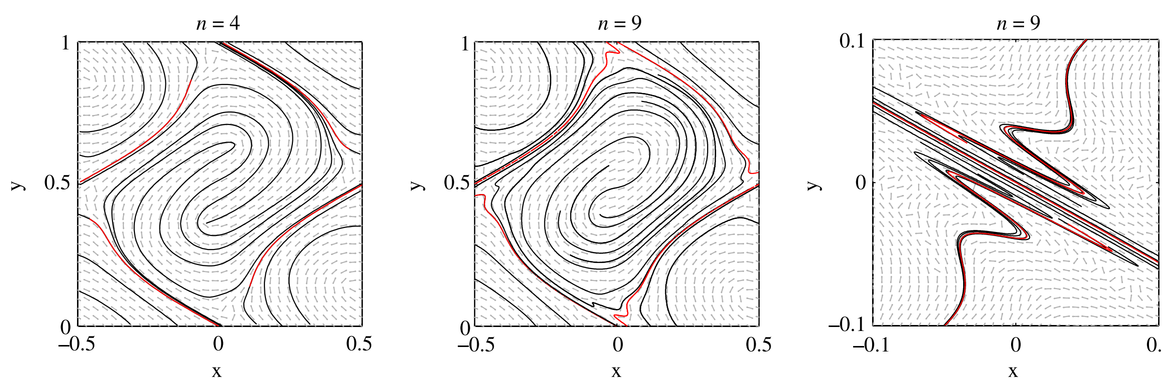

Fig. 11. Forward-hyperbolic barriers (red curves) reconstructed from $n = 4$ and $n = 9$ iterations of the advection map P with $a = 0.2$. These barriers were located as super-minima of relative stretching among all strainline segments satisfying the cut-off condition $d_p^{\xi_1} \leq 10^{-3}$ pointwise. Some additional strainlines (black) are shown for reference. The unit eigenvector field ξ_1 is depicted at select positions, with double-headed arrows emphasizing its lack of a global orientation. The third plot shows a blow-up of the barrier obtained for $n = 9$ near the hyperbolic fixed point at $(0, 0)$. (For interpretation of the references to colour in this figure legend, the reader is referred to the web version of this article.)

the extracted forward-hyperbolic barriers (red curves) in Fig. 11 reconstructed from fewer iterations ($n = 4$ and $n = 9$) using our geodesic transport barrier theory.

As for elliptic barriers, Fig. 12 shows shearlines of the shear vector fields $\eta_\pm(x)$ obtained from $n = 15$ iterations of the advection map P. Those qualifying as elliptic barriers with $d_g^{\eta\pm} \leq \epsilon_{\eta_\pm} = 0.25$ are highlighted in green. The lower panel of the same figure shows the same computation using $n = 50$ iterations. Note that several closed shearlines in these figures still do not yet qualify as near-homogeneous barriers because $\langle d_g^{\eta\pm} \rangle > 0.25$ holds on them. Still, they already provide close approximations for KAM tori; some even highlight secondary KAM tori within the resonant islands.

A more detailed study of the convergence of our elliptic barrier reconstruction algorithm is shown in Figs. 13 and 14. Note that the more iterations are used in the reconstruction, the smaller the geodesic deviation becomes, and the closer the closed shearline becomes to an invariant curve. Generally, for geodesic deviations of the order $\langle d_g^{\eta\pm} \rangle \leq 0.25$, KAM tori and reconstructed elliptic barriers appear indistinguishable.

Finally, in Fig. 15, we show together the set of reconstructed hyperbolic and elliptic barriers. Gray curves indicate hyperbolic and elliptic barriers from the second, high-resolution phase portrait of P shown in Fig. 10. At this resolution, each reconstructed hyperbolic and elliptic barrier coincides with an observed barrier (stable manifold, unstable manifold, or KAM torus). A blow-up of the heteroclinic tangle on the right provides further confirmation of the accuracy of our barrier reconstruction.

We conclude that our geodesic transport theory provides highly accurate barriers using relatively low numbers of iterations of P. Simply iterating P for the same length of time does not provide the same quality or detail (compare the left panels of Figs. 10 and 15). Admittedly, the high accuracy of the geodesic theory comes at a higher computational cost relative to the cost of simply iterating the map P.

9. Example 2: Transport barriers in the chaotically forced Bickley jet

In our second example, we apply our geodesic transport theory to a spatially more complex, temporally aperiodic planar dynamical system. In this setting, no Poincare maps are available, and hence even an indirect visualization of transport barriers from advected initial conditions would be problematic. Indeed, there is no known frame or stroboscopic mapping sequence under which the barriers become steady.

Consider the two-dimensional incompressible flow defined by the stream function

$$\psi(x, y, t) = \psi_0(x, y) + \psi_1(x, y, t) \tag{44}$$

with

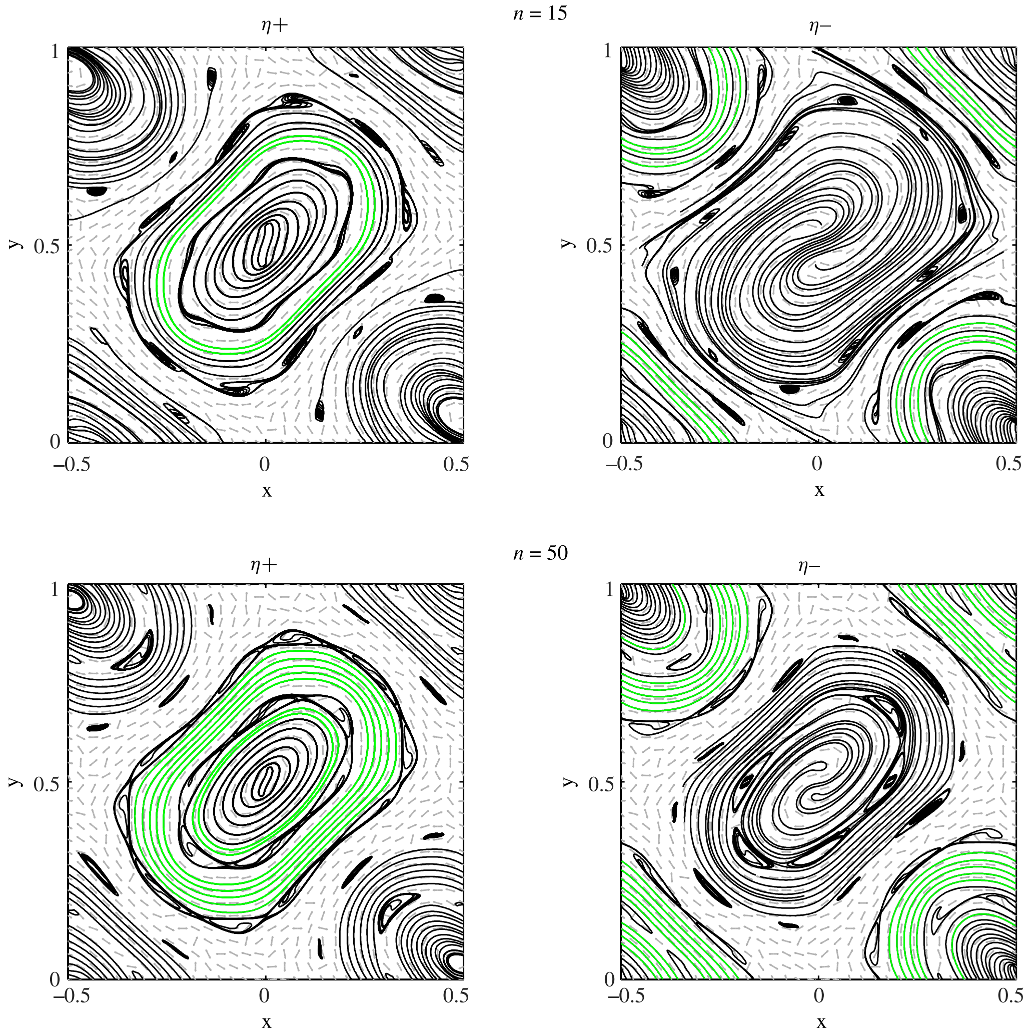

Fig. 12. Select shearlines (black) and elliptic transport barriers (green) with $\langle d_g^{\eta\pm}\rangle \le \epsilon_{\eta\pm} = 0.25$ for the advection map (43) with $a = 0.2$. Double-headed arrows indicate the $\eta_\pm$ direction fields. (For interpretation of the references to colour in this figure legend, the reader is referred to the web version of this article.)

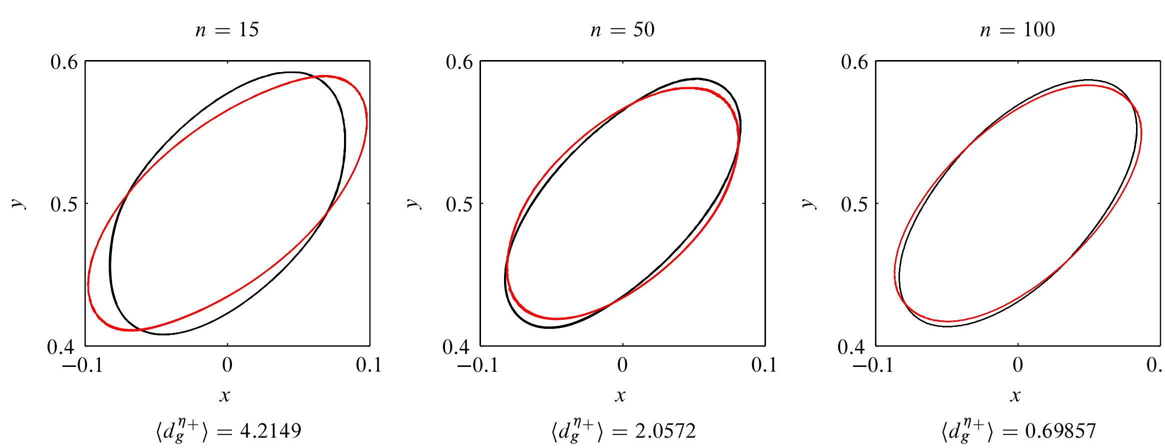

Fig. 13. A closed shearline (black) starting from a fixed initial position, reconstructed from increasingly longer iterations of P. Also shown the image of the shearline under one iteration of P. The mismatch between the black and red curves indicates the degree of non-invariance of the black curve. Convergence of the shearline to an invariant curve is also indicated by the gradual decrease in the shearline's average geodesic deviation $\langle d_g^{\eta+}\rangle$. (For interpretation of the references to colour in this figure legend, the reader is referred to the web version of this article.)

$$\psi_0(x, y) = c_3 y - UL_y \tanh\frac{y}{L_y} + \varepsilon_3 UL_y \operatorname{sech}^2\frac{y}{L_y}\cos k_3 x, \tag{45}$$

$$\psi_1(x, y, t) = UL_y \operatorname{sech}^2\frac{y}{L_y}\operatorname{Re}\left[\sum_{n=1}^{2}\varepsilon_n f_n(t)e^{ik_n x}\right], \tag{46}$$

$$k_n = 2n\pi/L_x. \tag{47}$$

We consider the periodic variable $x \in [0, 2\pi/L_x]$ as a zonal coordinate, and $y \in \mathbb{R}$ as a meridional coordinate. We choose the parameters in ψ as in [24]: $L_x = \pi a$, where $a = 6371$ km is the mean radius of the Earth; $U = 62.66\ \mathrm{ms}^{-1}$; $L_y = 1770$ km;

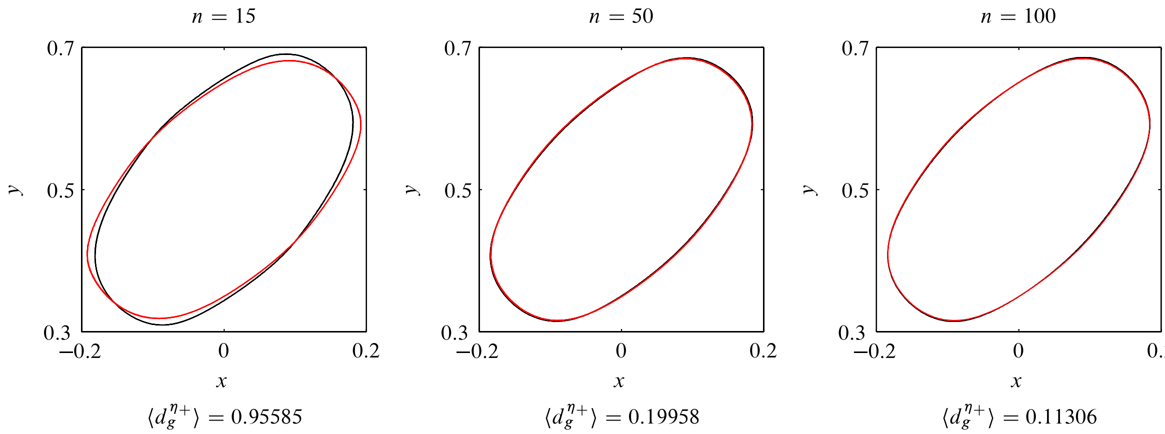

Fig. 14. Same as Fig. 13, but for a closed shearline of larger amplitude.

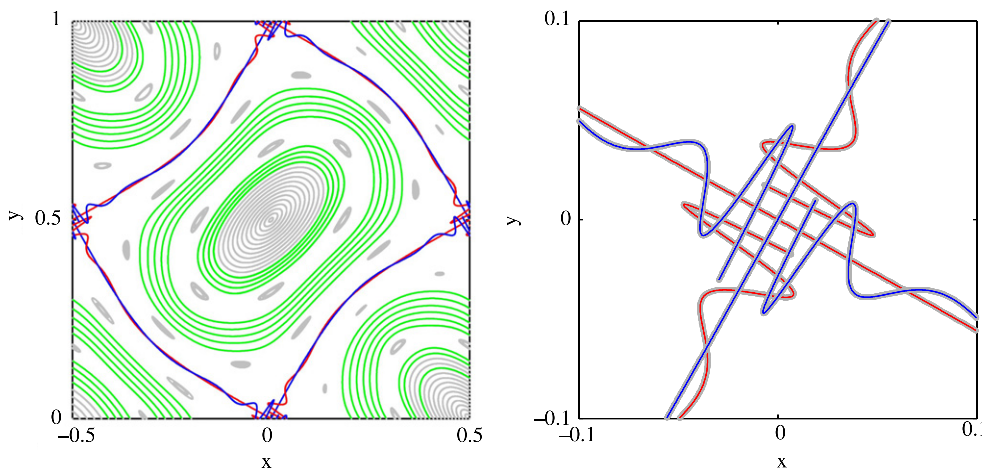

Fig. 15. Forward- and backward-hyperbolic barriers (red and blue), as well as elliptic barriers (green), obtained from the geodesic theory. The hyperbolic barriers were reconstructed using $n = 9$ iterations of the chaotic advection map (43) with $a = 0.2$. The barrier segments were truncated at points where their geodesic deviation $d_g^{\xi_1}$ reaches the cut-off value $\epsilon_{\xi_1} = 10^{-3}$. The elliptic barriers were obtained using $n = 100$ iterations of P, with average geodesic deviation $\langle d_g^{\eta+} \rangle \leq 0.25$. Gray curves indicate hyperbolic and elliptic barriers inferred from the higher-resolution phase portrait in the second panel of Fig. 10. Note that this phase portrait required a higher number of iterations to construct ($n = 14$ for the hyperbolic barriers and $n = 10^4$ for the elliptic barriers). (For interpretation of the references to colour in this figure legend, the reader is referred to the web version of this article.)

$c_3/U = 0.461$; $\varepsilon_1 = 0.075$; $\varepsilon_2 = 0.4$; $c_2/U = 0.205$. In that setting, ψ_0 represents a meandering eastward zonal jet (known as the Bickley jet [25,26]) which is flanked northward and southward by three stationary vortices produced by a wavenumber-3 Rossby wave. The unsteady streamfunction ψ_1 is a superposition of two x-periodic modes with time-dependent amplitudes, which decay to zero in the $\pm y$ direction. Fluid particle trajectories are generated by the unsteady velocity field

$$v(x, y, t) = \left(-\partial_y\psi, \partial_x\psi\right). \tag{48}$$

We consider the following choices for the perturbations streamfunction ψ_1:

(1) Time-periodic ψ_1 with ε_n at one tenth of the values used in [24], and with $f_n(t) = \exp(-i\sigma_n t)$, where $\sigma_1 = k_2(c_2 - c_3)$, with c_2 and c_3 as in [24], and $\sigma_2 = 2\sigma_1$. We only consider this case to produce a reference Poincare map for comparison with our results on the temporally aperiodic cases.

(2) Time-aperiodic ψ_1 with ε_n as in [24], and with $f_n(t)$ taken to be an appropriately rescaled solution of the forced–damped Duffing oscillator with parameters in the chaotic regime. Specifically, we let $f_n(t) = 7\varphi_n(2\pi\tau/5\sigma_2)/4 \max \varphi_n(\tau)$ where $\varphi_n(\tau)$ satisfies

$$\frac{d\varphi_1}{d\tau} = \varphi_2, \qquad \frac{d\varphi_2}{d\tau} = -\frac{1}{10}\varphi_2 - \varphi_1^3 + 11\cos\tau, \tag{49}$$

with initial conditions $\varphi_n(0) = 0$;

(3) Time-aperiodic ψ_1 with the same structure as in (2), but with a smaller amplitude equal to that chosen in case (1).

Fig. 16 shows the nature of time-dependence in cases (1)–(3).

As a general reference, Fig. 17 shows transport barriers obtained for case (1) (i.e., time-periodic forcing), obtained from iterations of the Poincaré map $F_{t_0}^{t_0+T}$ with $T = 4L_x/U$. This map was applied repeatedly to select initial conditions in the eddy regions, and to small circles of initial conditions around the perturbed hyperbolic fixed points.

We now turn to the analysis of the time-aperiodic perturbations for which barriers are not known and cannot be visualized through Poincaré maps. In all our computations, we use a uniform grid of 4096×1637 initial conditions to obtain high-resolution and accurate curves for transport barriers.

Fig. 18 shows forward-hyperbolic barriers obtained from the geodesic theory for the case of strong time-aperiodic perturbation (case (2)). The complexity of these barriers is notably higher than those observed in the weakly forced time-periodic phase portrait shown in Fig. 17.

The hyperbolic barriers fully penetrate the two rows of eddies, destroying the elliptic barriers observed in Fig. 17. Parabolic

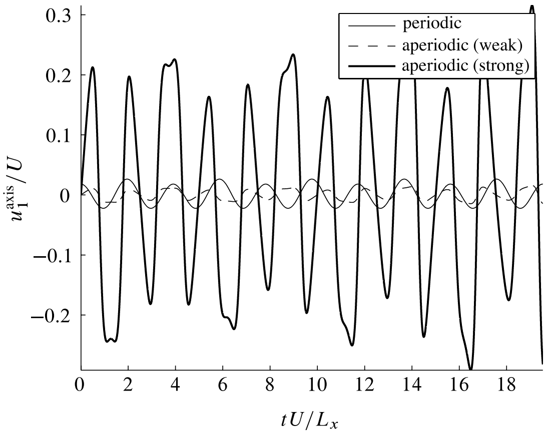

Fig. 16. The three types of zonal perturbation velocities considered, all evaluated at a point on the axis of the background meandering zonal jet.

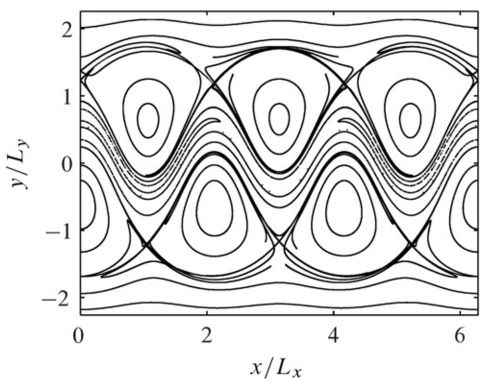

Fig. 17. Phase portrait of the Poincaré map $F_{t_0}^{t_0+T}$ for the time-periodic Bickley jet (case (1)) with $t_0 = 0$ and $T = 4L_x/U$.

barriers with low geodesic deviation ($\langle d_g^{\eta\pm}\rangle \le 0.0015$) do not exist either. This is further illustrated in Fig. 19, which shows a superposition of forward- and backward-hyperbolic barriers obtained from the geodesic theory at $t_0 = 0$.

By contrast, the elliptic regions are not destroyed in the case of weaker chaotic forcing (case (3)), as seen in Fig. 20. Convergence to generalized KAM tori (closed green curves) and generalized shear jets (open green curves) is apparent for increasing temporal length T for the data set.

In general, $T = 20L_x/U$ emerges as the minimal time scale needed for the robust identification of shear barriers. For this length of data, Fig. 21 illustrates that averaged geodesic deviation values satisfying $\langle d_g^{\eta\pm}\rangle \le 0.0015$ are effective in isolating generalized KAM-type and jet-type structures from open spiraling strainlines. The latter strainlines also remain close to least-stretching geodesics but do not act as closed boundaries of elliptic regions.

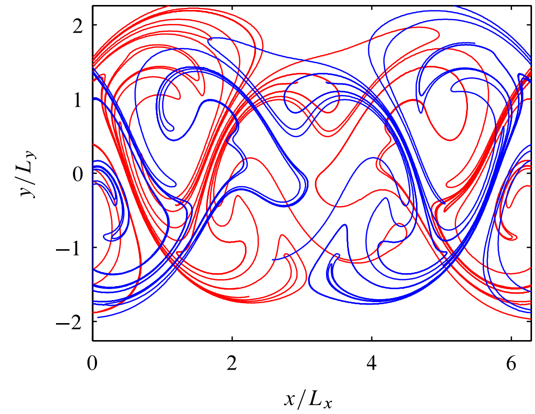

Fig. 19. Forward- and backward-hyperbolic barriers (red and blue) at time $t_0 = 0$ obtained from the geodesic theory for Bickley jet with strong chaotic forcing (case (2)). We used the forward time interval $[t_0, t_0 + T]$ and the backward-time interval $[t_0, t_0 - T]$ in this analysis with $T = 4L_x/U$. We again let $\epsilon_{\xi_1} = 10^{-6}$ for the admissible bound on the pointwise geodesic deviation curvature along hyperbolic barriers. (For interpretation of the references to colour in this figure legend, the reader is referred to the web version of this article.)

Finally, Fig. 22 shows a composite picture of transport barriers obtained from our geodesic theory for the Bickley jet with weak chaotic forcing. Note that the robust extraction of elliptic barriers required a time interval that is about five times the minimal time scale needed for a robust detection of hyperbolic barriers. This is because shear barriers only prevail as minimally stretching material lines on longer time intervals due to the algebraic growth of material length in shear regions vs. exponential growth in high-strain regions.

While the location of the barriers is robust for times beyond $T = 20L_x/U$ and for geodesic deviation values $\langle d_g^{\eta\pm}\rangle \le 0.0015$, resolving all details of the barriers in the current, chaotically forced setting proves to be a challenge. For instance, one of the closed elliptic barriers centered roughly around $(x/L_x, y/L_y) = (4.1, -0.6)$ in Fig. 22 appears to turn around and form a lobe. This is due to numerical errors in the computation of the underlying strainlines over the relatively long time interval $[0, 20L_x/U]$. The artificial lobe disappears once the spatial resolution in our computations is doubled in this elliptic region (cf. the right panel in Fig. 22).

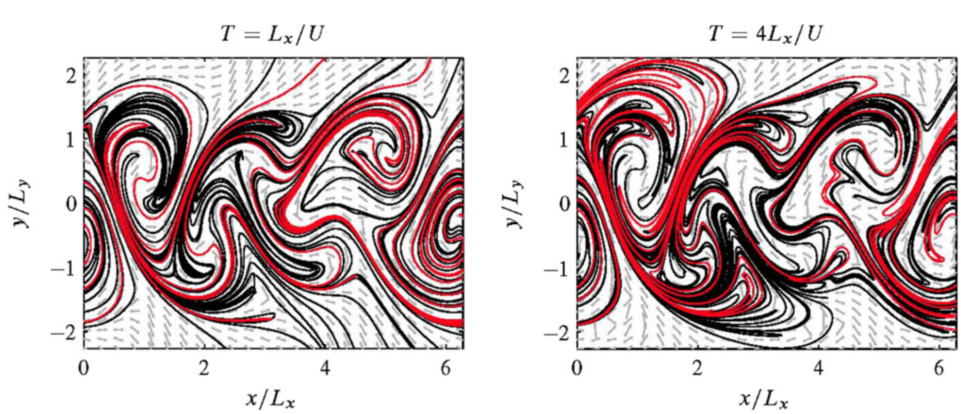

Fig. 18. Forward-time hyperbolic barriers (red) obtained from the geodesic theory at time $t_0 = 0$ for the Bickley jet with strong chaotic forcing (case (2)) over $[t_0, t_0 + T]$, for two different choices of the interval length T. The pointwise admissible upper bound on the geodesic deviation is chosen to be $\epsilon_{\xi_1} = 10^{-6}$. Also shown are some additional strainlines (black) and the minimum strain eigenvector field $\xi_1(x, y)$ (gray) for reference. (For interpretation of the references to colour in this figure legend, the reader is referred to the web version of this article.)

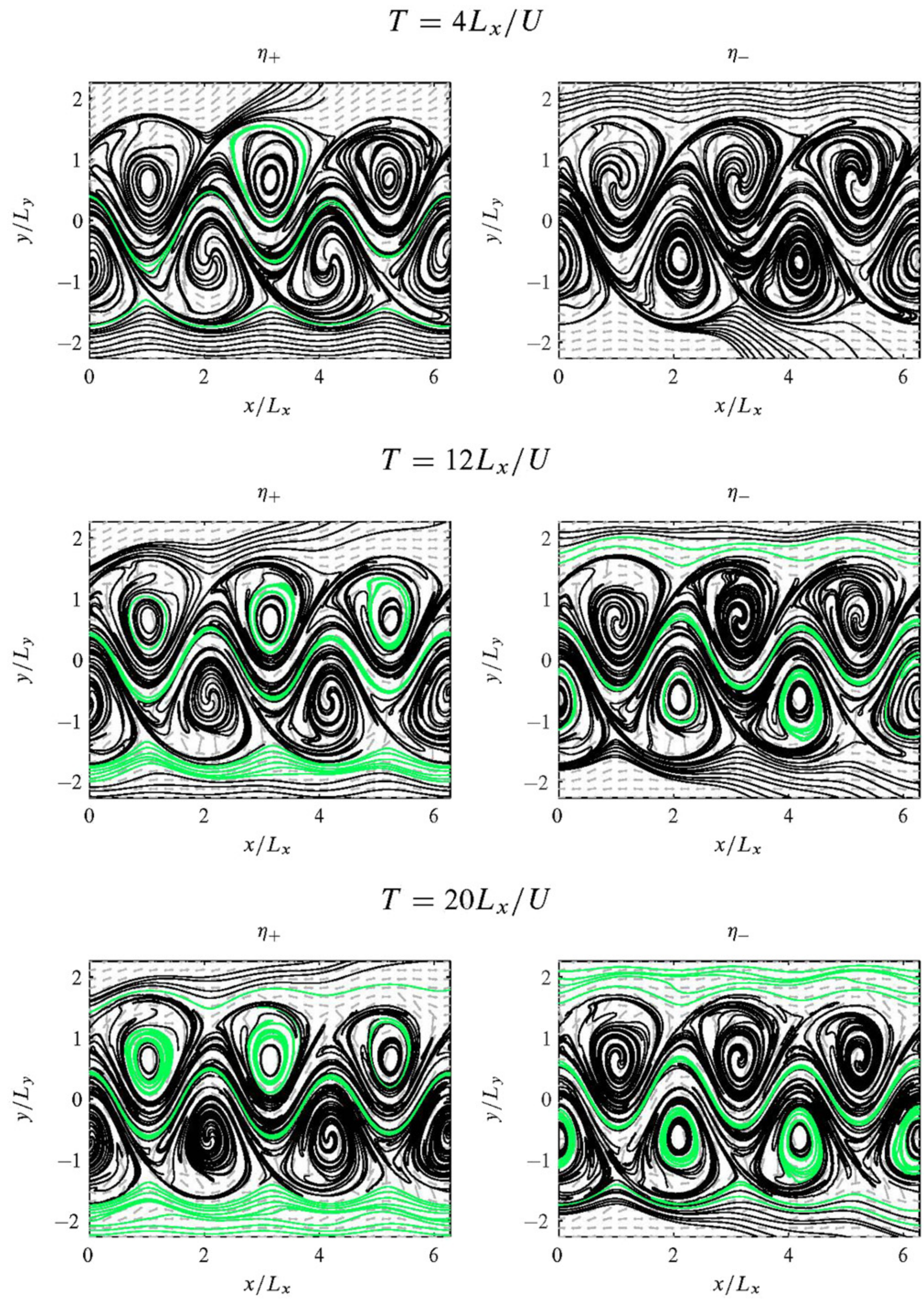

Fig. 20. Elliptic and parabolic barriers (green) obtained from the geodesic theory for the Bickley jet with weak chaotic forcing (case (3)). The barriers are extracted at $t_0 = 0$ for three different lengths of the time interval $[t_0, t_0 + T]$, with average geodesic deviation values satisfying the bound $\langle d_g^{\eta\pm} \rangle \leq 0.0015$. (For interpretation of the references to colour in this figure legend, the reader is referred to the web version of this article.)

10. Conclusions

We have developed a unified theory of transport barriers for two-dimensional, non-autonomous dynamical systems. We have obtained that the most influential barriers are locally most compressing or most shearing material lines that are closely shadowed by least-stretching geodesics of the metric induced by Cauchy–Green strain tensor. These barriers, strainlines and shearlines, can be found as trajectories of first-order ODEs.

We have classified transport barriers as forward- and backward-time hyperbolic barriers and shear barriers. The two types of hyperbolic barriers are formed by forward-time and backward-time strainlines with small pointwise C^2-distance (geodesic deviation) from least-stretching Cauchy–Green geodesics. We note that hyperbolic Lagrangian Coherent Structures (LCSs) have also been identified recently as strainline segments that are more locally repelling than their neighbors (cf. [20]). Although this related result on LCSs follows from a different approach, it does signal an intrinsic connection between hyperbolic LCSs and the hyperbolic transport barriers introduced in this paper.

In incompressible flows, shear barriers turned out to have the same arclength at time $t_0 + T$ as they do at time t_0. This allowed us to further classify shear barriers as parabolic and elliptic barriers. Parabolic barriers are open shearlines with small average geodesic deviation, representing a generalization of shear jets to temporally aperiodic flows. By contrast, elliptic barriers

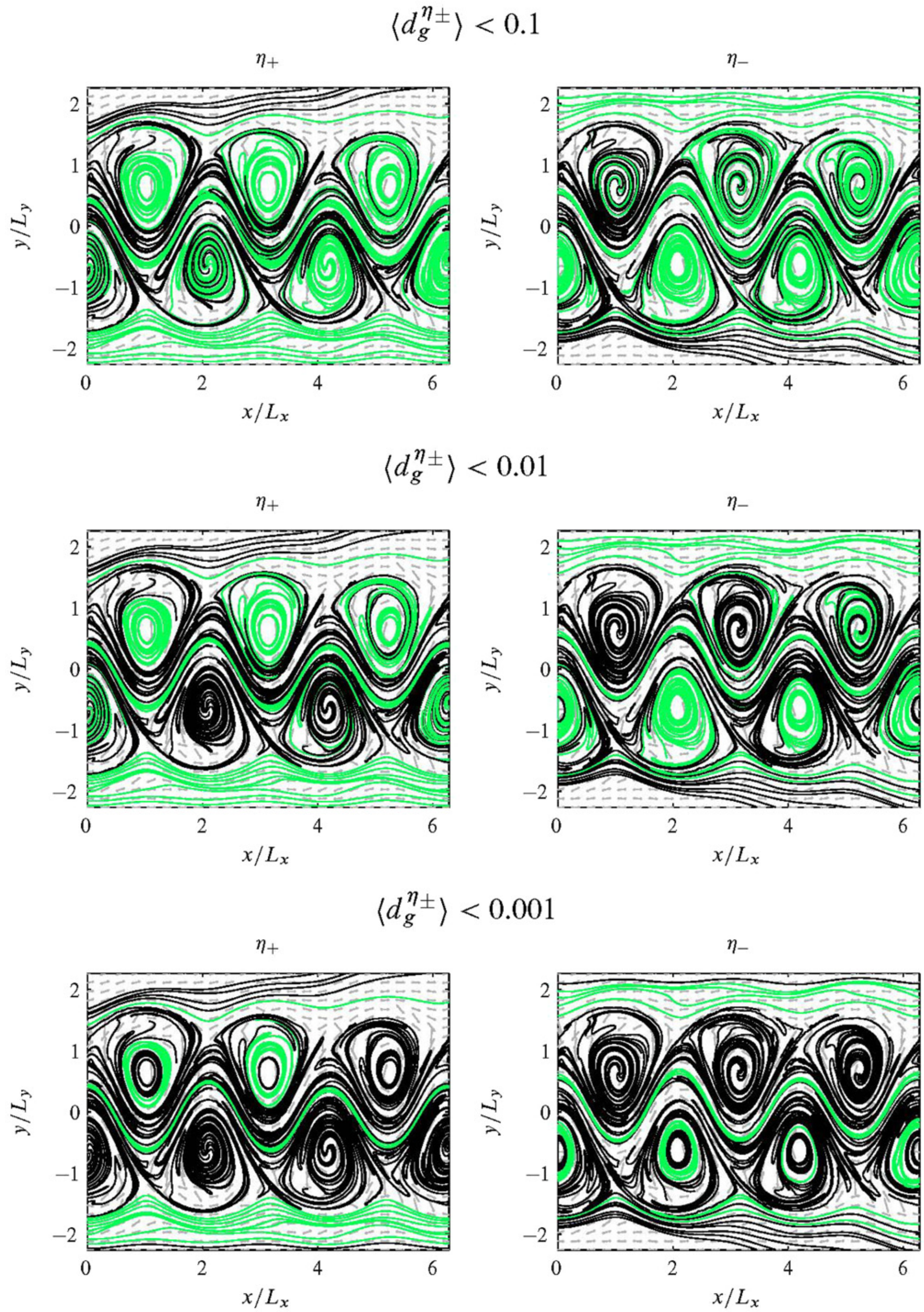

Fig. 21. Isolation of elliptic barriers from spiraling shearlines for decreasing bounds on the average geodesic deviation $\langle d_g^{\eta\pm} \rangle$ in the Bickley jet with weak chaotic forcing (case (3)).

are closed shearlines with small geodesic deviation, playing the role of generalized KAM curves (or Lagrangian eddy barriers) in general, non-autonomous dynamical systems. Closed shearlines are not simply local minimizers of material stretching over the time interval $[t_0, t_0 + T]$: they in fact have the same arclength at time $t_0 + T$ as they do at time t_0.

Transport-barrier computations can be considered converged once geodesic deviation on the barriers decreases below an *a priori* chosen error bound. This provides a quantitative criterion for optimal stopping times in the integration of trajectories of Eq. (1), expediting the real-time detection of transport barriers in critical situations, such as the tracking of an evolving environmental contamination pattern [27].

Our unified approach identifies barriers to phase space transport, but does not offer a direct way to quantify transport itself. The hyperbolic barriers we identify, however, are geometric templates for a possible extension of geometric transport theories from two-dimensional maps and time-periodic ODEs [28–30] to time-aperiodic planar flows.

Higher-dimensional extensions of our theory should involve the construction of locally least-stretching codimension-one material surfaces. Hyperbolic barriers in that context are expected to be hypersurfaces that are tangent to the first $n - 1$ eigenvectors of the Cauchy–Green strain tensor, as is the case for hyperbolic LCSs in n-dimensions [11]. The existence of such surfaces, however, is not a priori guaranteed and hence requires further analysis.

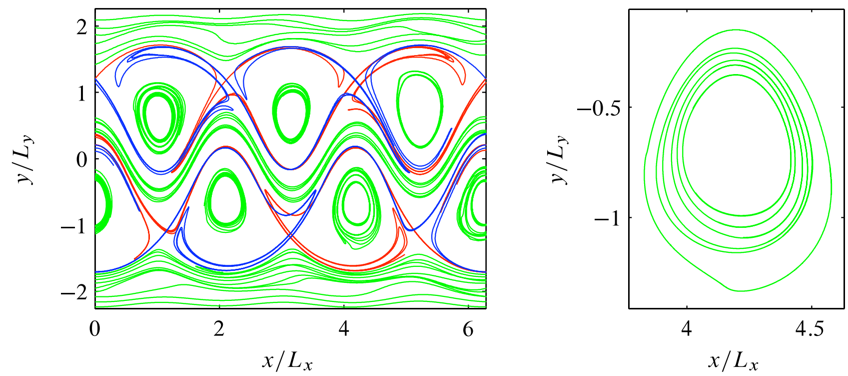

Fig. 22. Forward- and backward-hyperbolic barriers (red and blue), as well as elliptic barriers (green), obtained from the geodesic theory for the Bickley jet with weak chaotic forcing. The hyperbolic barriers were reconstructed using the velocity field up to the time $T = 4L_x/U$; the elliptic and parabolic barriers were obtained using the velocity field up to the time $T = 20L_x/U$. The panel on the right shows the blow-up of a single elliptic region, with the computations performed at twice the original resolution. (For interpretation of the references to colour in this figure legend, the reader is referred to the web version of this article.)

To our knowledge, the theory developed here reveals transport barriers in general two-dimensional dynamical systems at a level of rigor and detail that has not been achieved by prior methods. An efficient and accurate implementation of this theory undoubtedly requires an investment in computational resources, as we have seen in the two examples discussed in this paper. However, the ever-increasing availability of multi-core CPUs and graphics processing units (GPUs) brings the necessary processing power and memory within reach.

Indeed, orders of magnitude performance improvements have been reported in the integration of arrays of trajectories – the most resource-hungry part of our approach – after the introduction of parallel computation and GPUs [31,32]. This provides a compelling reason for investing in the necessary coding and hardware, enabling a fast yet accurate and objective detection of transport barriers.

Acknowledgments

We thank Ronny Peikert and Xavier Tricochet for their remarks and for the references they provided on tensor lines. We also thank Darryl Holm, Gábor Stépán, Alan Weinstein and the anonymous referees for their helpful comments and suggestions. We are grateful to Mohammad Farazmand for checking the details of several derivations in this paper. G.H. acknowledges support by the Canadian NSERC under grant 401839-11. F.J.B.V. acknowledges support by the US NSF under grant CMG0825547, by NASA under grant NNX10AE99G, and by British Petroleum under the Gulf of Mexico Research Initiative.

Appendix A. Lagrangian shear and its locally maximal directions

A.1. Definition of Lagrangian shear

We adapt and further develop the notion of Lagrangian shear along a material surface from the three-dimensional context in [33], where this frame-independent description of material shear was apparently first introduced.

Consider an evolving material line γ_t. At an initial condition $x_0 \in \gamma_{t_0}$, a unit normal n_0 to the initial material curve γ_{t_0} can be expressed in terms of a unit tangent vector $e_0 \in T_{x_0}\gamma_{t_0}$ as

$$n_0 = \Omega e_0,$$

with the orthogonal rotation matrix Ω defined in (6). Further note that the tangent space $T_{x_t}\gamma_t$ along the trajectory $x_t = x(t; t_0, x_0)$ in the material line γ_t is the linear span of $DF^t_{t_0}(x_0)e_0$. Therefore,

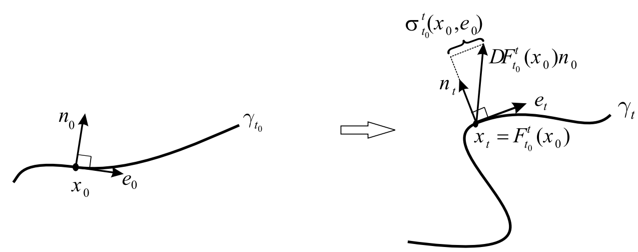

Fig. 23. The definition of the Lagrangian shear $\sigma^t_{t_0}$.

a unit tangent vector in $T_{x_t}\gamma_t$ can be selected as $e_t = DF^t_{t_0}(x_0)e_0/\left|DF^t_{t_0}(x_0)e_0\right|$.

We define the *Lagrangian shear* $\sigma^t_{t_0}$ as the normal projection of the linearly advected unit normal $DF^t_{t_0}(x_0)n_0$ onto the advected unit tangent e_t, as shown in Fig. 23. This definition of finite-time Lagrangian shear along γ_t naturally complements the definition of finite-time normal repulsion $\rho^t_{t_0}$ along γ_t given in [11], with $\rho^t_{t_0}$ being the normal projection of $DF^t_{t_0}(x_0)n_0$ onto the local unit normal n_t of γ_t at the point x_t.

More specifically, without explicit reference to the underlying material line γ_t, we can compute $\sigma^t_{t_0}$ with respect to any initial point $x_0 \in U$ and any initial tangent direction e_0 as

$$\sigma^t_{t_0}(x_0, e_0) = \left\langle e_t, DF^t_{t_0}(x_0)n_0\right\rangle = \frac{\left\langle DF^t_{t_0}(x_0)e_0, DF^t_{t_0}(x)\Omega e_0\right\rangle}{\left|DF^t_{t_0}(x_0)e_0\right|} \tag{50}$$

$$= \frac{\left\langle \Omega e_0, C^t_{t_0}(x_0)e_0\right\rangle}{\sqrt{\left\langle e_0, C^t_{t_0}(x_0)e_0\right\rangle}}. \tag{51}$$

Positive $\sigma^t_{t_0}(x_0, e_0)$ values signal positive (clockwise) shear in the local coordinate frame $[\xi_1(x_0), \xi_2(x_0)]$; negative $\sigma^t_{t_0}(x_0, e_0)$ values signal negative (counterclockwise) shear in the same frame.

A.2. Directions and magnitude of maximal Lagrangian shear

We seek local extrema of $\sigma^t_{t_0}(x, \cdot)$ as unit vectors of the form

$$e_0 = \alpha\xi_1 + \beta\xi_2, \qquad \alpha^2 + \beta^2 = 1, \tag{52}$$

with the constants $\alpha(x)$ and $\beta(x)$ to be determined. Substituting (52) into (50), we obtain

$$\sigma(x, \alpha, \beta) = \frac{\left\langle \Omega\left(\alpha\xi_1 + \beta\xi_2\right), C^t_{t_0}\left[\alpha\xi_1 + \beta\xi_2\right]\right\rangle}{\sqrt{\left\langle \alpha\xi_1 + \beta\xi_2, C^t_{t_0}\left[\alpha\xi_1 + \beta\xi_2\right]\right\rangle}}$$

$$= \frac{\left\langle (\alpha\xi_2 - \beta\xi_1), C_{t_0}^t [\alpha\xi_1 + \beta\xi_2] \right\rangle}{\sqrt{\left\langle \alpha\xi_1 + \beta\xi_2, C_{t_0}^t [\alpha\xi_1 + \beta\xi_2] \right\rangle}}$$
$$= \frac{\alpha\beta (\lambda_2 - \lambda_1)}{\sqrt{\alpha^2\lambda_1 + \beta^2\lambda_2}}.$$

At extrema of $\sigma(x, \cdot)$, we have

$$\frac{\partial\sigma}{\partial\alpha} = \frac{\beta(\lambda_2 - \lambda_1)\left(\alpha^2\lambda_1 + \beta^2\lambda_2\right) - \alpha\beta(\lambda_2 - \lambda_1)\alpha\lambda_1}{\left(\alpha^2\lambda_1 + \beta^2\lambda_2\right)^{3/2}} = 2\lambda\alpha,$$
$$\frac{\partial\sigma}{\partial\beta} = \frac{\alpha(\lambda_2 - \lambda_1)\left(\alpha^2\lambda_1 + \beta^2\lambda_2\right) - \alpha\beta(\lambda_2 - \lambda_1)\beta\lambda_2}{\left(\alpha^2\lambda_1 + \beta^2\lambda_2\right)^{3/2}} = 2\lambda\beta,$$

where λ is a Lagrange multiplier introduced for the constraint $\alpha^2 + \beta^2 = 1$. Equivalently, we have

$$(\lambda_2 - \lambda_1)\frac{\beta^3\lambda_2}{\left(\alpha^2\lambda_1 + \beta^2\lambda_2\right)^{3/2}} = 2\lambda\alpha,$$
$$(\lambda_2 - \lambda_1)\frac{\alpha^3\lambda_1}{\left(\alpha^2\lambda_1 + \beta^2\lambda_2\right)^{3/2}} = 2\lambda\beta,$$

or

$$\frac{\beta}{\alpha} = \pm\sqrt[4]{\frac{\lambda_1}{\lambda_2}}.$$

Combined with the constraint $\alpha^2 + \beta^2 = 1$, this last equation gives the following two extremum directions for e_0:

$$\eta_\pm = \sqrt{\frac{\sqrt{\lambda_2}}{\sqrt{\lambda_1} + \sqrt{\lambda_2}}}\xi_1 \pm \sqrt{\frac{\sqrt{\lambda_1}}{\sqrt{\lambda_1} + \sqrt{\lambda_2}}}\xi_2. \tag{53}$$

Substituting these vectors into the expression (50) for $\sigma_{t_0}^t$ gives the extremum values

$$\sigma_{t_0}^t(x, \eta_\pm(x)) = \pm\frac{\sqrt{\lambda_2(x)} - \sqrt{\lambda_1(x)}}{\sqrt[4]{\lambda_1(x)\lambda_2(x)}}. \tag{54}$$

It is simple to verify that $\left|\sigma_{t_0}^t(x, \cdot)\right|^2$ admits a local maximum along the vectors $\eta_\pm(x)$. Therefore, the values in (54) represent locally maximal positive and negative Lagrangian shear values.

A.3. An alternative characterization of directions of maximum Lagrangian shear

Note that

$$\left\langle \eta_\pm, C_{t_0}^t \eta_\pm \right\rangle = \frac{\sqrt{\lambda_2}\lambda_1}{\sqrt{\lambda_1} + \sqrt{\lambda_2}} + \frac{\sqrt{\lambda_1}\lambda_2}{\sqrt{\lambda_1} + \sqrt{\lambda_2}}$$
$$= \sqrt{\lambda_1\lambda_2} = \sqrt{\det C_{t_0}^t} = \det DF_{t_0}^t, \tag{55}$$

thus the shear vectors $\eta_\pm$ are stretched by exactly the same factor as infinitesimal areas under the action of $DF_{t_0}^t$. As long as $\lambda_1 \neq \lambda_2$, there are precisely two subspaces with this stretching property, as one concludes from the analysis of the quadratic form $\left\langle \eta_\pm, C_{t_0}^t \eta_\pm \right\rangle$. Consequently, the two subspaces spanned by shear vectors coincide with the two subspaces in which vectors are stretched by a factor of $\det DF_{t_0}^t$.

Substituting $\eta_\pm^1 = \cos\phi$ and $\eta_\pm^2 = \sin\phi$ with $\phi \in [0, 2\pi)$ into (55), we obtain an alternative equation for the shear vector fields in terms of the angle ϕ they enclose with the x axis:

$$C_{11}\cos^2\phi + 2C_{12}\sin\phi\cos\phi + C_{22}\sin^2\phi = \det DF_{t_0}^t. \tag{56}$$

Taking the square of this equation yields

$$4C_{12}^2 \sin^2\phi\left(1 - \sin^2\phi\right)$$
$$= \left[\det DF_{t_0}^t - C_{11}\left(1 - \sin^2\phi\right) - C_{22}\sin^2\phi\right]^2,$$

which, in turn, leads to a quadratic equation for $\sin^2\phi$ in the form

$$\left[2\det C - \|C\|^2\right]\sin^4\phi + 2\left[\det DF_{t_0}^t(C_{22} - C_{11}) + C_{12}^2 + \det C + C_{11}^2\right]\sin^2\phi - \left[\det DF_{t_0}^t - C_{11}\right]^2 = 0. \tag{57}$$

For incompressible flows, (57) simplifies to

$$\left[2 - \|C\|^2\right]\sin^4\phi + 2\left[(1 + C_{22} - C_{11}) + C_{12}^2 + C_{11}^2\right]\sin^2\phi - [1 - C_{11}]^2 = 0. \tag{58}$$

This formula is useful in identifying the direction of maximal Lagrangian shear in specific examples (see, e.g., Appendix D.2.3).

A.4. Comparison of Lagrangian shear with shear strain in continuum mechanics

We conclude this Appendix by comparing the Lagrangian shear $\sigma_{t_0}^t(x_0, e_0)$ defined is (50) with the classic notion of Lagrangian shear [14], which is associated with the change in the angle between two initially orthogonal vectors, such as e_0 and n_0, under the linearized flow map $DF_{t_0}^t(x_0)$. The *sine* of this angle change is equal to the *cosine* enclosed by the advected vectors, given be the shear strain measure

$$\hat\sigma_{t_0}^t(x_0, e_0) = \frac{\left\langle e_t, DF_{t_0}^t(x_0)n_0 \right\rangle}{\left|DF_{t_0}^t(x_0)e_0\right|\left|DF_{t_0}^t(x_0)n_0\right|} \tag{59}$$
$$= \frac{\left\langle \Omega e_0, C_{t_0}^t(x_0)e_0 \right\rangle}{\sqrt{\left\langle e_0, C_{t_0}^t(x_0)e_0 \right\rangle}\sqrt{\left\langle \Omega e_0, C_{t_0}^t(x_0)\Omega e_0 \right\rangle}}. \tag{60}$$

This classic shear strain measure is well-known to be maximal in norm along the directions

$$\hat\eta_\pm = \frac{1}{\sqrt{2}}(\xi_1 \pm \xi_2),$$

which are always at 45° angles from the eigenvectors of the Cauchy–Green strain tensor [14]. While of clear mechanical significance, these directions do not capture shear in a dynamical sense. For instance, $\hat\eta_\pm$ do not even align with dynamical shear-type barriers in steady parallel shear flows (cf. Appendix D.2 with $u(y, t) \equiv u(y)$).

Appendix B. Poof of Theorem 1

Statement (i) follows by observing from (3) that the stretched arclength $l_{t_0}^t(\gamma_0)$ can be viewed as the length of γ_0 under a Riemannian metric c defined in (19). As a result, extrema of the functional $l_{t_0}^t$ are geodesics on (U, c).

To prove statement (ii), observe that for hyperbolic and shear barriers, Eqs. (10) and (11) imply that

$$\delta l_{t_0}^t(\gamma_0)[h] = \sqrt{2}\int_{s_1}^{s_2}\left[\partial_r\sqrt{L(r, r')} - \frac{d}{ds}\partial_{r'}\sqrt{L(r, r')}\right]\cdot h\,ds = 0 \tag{61}$$

must hold for all perturbations $h(s)$ consistent with the boundary conditions (15) or (17). Since all these possible boundary conditions include the case of fixed boundary conditions $(h(s_1) =$

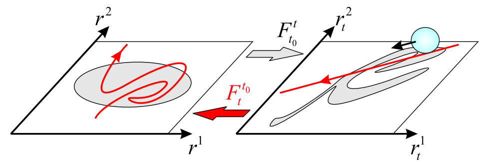

Fig. 24. Cauchy–Green geodesics are preimages of orbits of a point mass moving on the deformed flow configuration labeled by the coordinates (r_t^1, r_t^2). The Lagrangian and Hamiltonian equations of motion, (20) and (22), describe this particle motion in terms of the coordinates (r^1, r^2) parameterizing the initial configuration of the flow.

$h(s_2) = 0$), transport barriers are also local minimizers of the arclength functional $l_{t_0}^t$ under fixed boundary conditions. As a consequence, the classic Maupertius principle (see, e.g., [34]) implies that transport barriers further minimize the energy functional

$$E_{t_0}^t(\gamma_0) = \int_{s_1}^{s_2} L(r(s), r'(s))ds \tag{62}$$

under fixed boundary conditions. Applying the fundamental lemma of the calculus of variations to the energy functional (62) then leads to the classic Euler–Lagrange equations (20) for geodesics (see, e.g., [35]).

These equations admit a non-degenerate first integral

$$H = \langle r', \partial_{r'} L\rangle - L \equiv L(r(s), r'(s)). \tag{63}$$

Statement (iii) of Theorem 1 then follows by direct calculation using this Hamiltonian.

Appendix C. Mechanical analogy for Cauchy–Green geodesics

Consider an imaginary free particle of unit mass, moving over the deformed configuration $F_{t_0}^t(U)$, with its path marked as $r_t(s)$. The kinetic energy of such a particle is just $T(r_t') = \frac{1}{2}\langle r_t', r_t'\rangle$. Now describe the motion of this imaginary particle using the generalized coordinate $r = F_t^{t_0}(r_t)$, i.e., the initial position of the particle in the flow generated by $F_{t_0}^t$. A direct calculation using (22) and (23) gives

$$\begin{aligned} T(r_t') &= \frac{1}{2}\langle r_t', r_t'\rangle = \frac{1}{2}\left\langle DF_{t_0}^t r', DF_{t_0}^t r'\right\rangle \\ &= \frac{1}{2}\left\langle r', C_{t_0}^t r'\right\rangle = \frac{1}{2}\left\langle \left[C_{t_0}^t(r)\right]^{-1} p, C_{t_0}^t\left[C_{t_0}^t(r)\right]^{-1} p\right\rangle \\ &= \frac{1}{2}\left\langle p, \left[C_{t_0}^t(r)\right]^{-1} p\right\rangle = H(r,p). \end{aligned}$$

Therefore, the Hamiltonian (23) can also be viewed as the Hamiltonian of a freely moving particle on $F_{t_0}^t(U)$, with the preimage r of the particle under the flow map used as generalized coordinate, and with the generalized momentum vector p canonically conjugate to r. Since a free particle moves on straight lines of the planar region $F_{t_0}^t(U)$, the Cauchy–Green geodesics $r(s)$ are always preimages of straight lines under the flow map $F_t^{t_0}$ (cf. Fig. 24). These straight lines are of the form given in (24).

We note that beyond the analogy discussed above with classical mechanical systems, arclength-minimizing functionals of the type (3) also appear in Fermat's principle for optical ray propagation in anisotropic media [36]. In that case, however, the equivalent of the matrix $DF_{t_0}^t$ – the inverse refractive index matrix – is typically not a gradient, and hence the analogue of the Cauchy–Green metric is not a pull-back metric.

Appendix D. Examples of homogeneous transport barriers

Below we review two simple classes of unsteady flows in which homogeneous transport barriers do exist, and coincide with transport barriers one would intuitively identify for these flows. For ease of notation, we will lower the upper indices of the variables r^i (i.e., write r_i instead), without changing the position of any other index; the summation convention over repeated indices also remains in effect.

D.1. Example: Homogeneous transport barriers in linear flows

For an unsteady linear flow

$$\dot{x} = A(t)x, \quad A(t) \in \mathbb{R}^{2\times 2}, \tag{64}$$

the normalized fundamental matrix solution $\Phi(t, t_0)$ can be used to obtain the expressions

$$F_{t_0}^t(x_0) = \Phi(t,t_0)x_0, \qquad DF_{t_0}^t = \Phi(t,t_0),$$
$$C_{t_0}^t = \Phi^T(t,t_0)\Phi(t,t_0).$$

Since $C_{t_0}^t$ does not depend on the initial condition x_0, the strain eigenvalue fields λ_1 and λ_2, as well as the corresponding eigenvector fields, ξ_1 and ξ_2, are globally constant for any fixed times t_0 and t.

Two simple cases of (64) are hyperbolic and elliptic steady linear flows, described by the constant coefficient matrices

$$\tilde{A} = \begin{pmatrix} 1 & 0 \\ 0 & -1 \end{pmatrix}, \qquad \hat{A} = \begin{pmatrix} 0 & 1 \\ -1 & 0 \end{pmatrix}, \tag{65}$$

respectively. These flows have explicitly computable Cauchy–Green strain tensors of the form

$$\tilde{C}_{t_0}^t = \begin{pmatrix} e^{2(t-t_0)} & 0 \\ 0 & e^{-2(t-t_0)} \end{pmatrix}, \qquad \hat{C}_{t_0}^t = \begin{pmatrix} 1 & 0 \\ 0 & -1 \end{pmatrix}. \tag{66}$$

D.1.1. Cauchy–Green geodesics

Because of the constancy of $C_{t_0}^t$ in x_0, all Christoffel symbols in the Euler–Lagrange equations (20) vanish. The equations for Cauchy–Green geodesics simplify to $r'' = 0$, yielding solutions that are all straight lines of the form

$$\begin{aligned} r_1(s) &= r_1(0) + s r_1'(0), \\ r_2(s) &= r_2(0) + s r_2'(0). \end{aligned} \tag{67}$$

D.1.2. Homogeneous hyperbolic barriers

All trajectories of the constant vector field ξ_1 are straight lines, and hence are contained in the geodesic family (67). In particular, the one-parameter family of lines

$$r(s) = r(0) + s\xi_1$$

are all Cauchy–Green geodesics that are tangent to ξ_1 at each of their points, and hence qualify as homogeneous hyperbolic transport barriers. This is consistent with the results in [11], where these parallel lines were characterized as Weak Lagrangian Coherent Structures (WLCSs). In our current context, the "weakness" of these barriers is seen from the fact that their parallel translations yield other geodesics (parallel lines) whose subsets shrink at precisely the same rate. In technical terms, this means that the Euler–Lagrange solutions in (67) are only stationary points, as opposed to strict local minima, for the length functional $l_{t_0}^t$.

For the steady saddle flow considered in (65), we obtain that $\tilde{\xi}_1$ is aligned with the stable manifold (y axis) of the origin, and hence all lines parallel to the y axis are homogeneous hyperbolic barriers (or WLCSs), as already noted in [11]. By contrast, for the symmetric center flow defined by $\hat{A}$, the weaker strain eigenvector $\hat{\xi}_1$ is undefined, because $\hat{C}_{t_0}^t$ is the identity matrix. Therefore, as expected, a steady linear center flow admits no hyperbolic transport barriers.

D.1.3. Homogeneous shear barriers

Again, all trajectories of the constant shear vector fields $\eta_\pm = \sqrt{\frac{\sqrt{\lambda_2}}{\sqrt{\lambda_1}+\sqrt{\lambda_2}}}\xi_1 \pm \sqrt{\frac{\sqrt{\lambda_1}}{\sqrt{\lambda_1}+\sqrt{\lambda_2}}}\xi_2$ are straight lines, coinciding with the two families of geodesics given by

$$r_\pm(s) = r(0) + s\eta_\pm.$$

Both families mark homogeneous transport barriers at time $t_0 = 0$. As the time t increases, the barriers $\gamma_t = F_{t_0}^t\left(\{r_\pm(s)\}_{s=s_1}^{s_2}\right)$ form rotating material lines along which maximal shear arises.

Specifically, for the steady saddle flow considered in (65), we obtain

$$\tilde{\eta}_\pm = \frac{1}{\sqrt{1+e^{-2(t-t_0)}}}\begin{pmatrix}0\\1\end{pmatrix} \pm \frac{1}{\sqrt{1+e^{2(t-t_0)}}}\begin{pmatrix}1\\0\end{pmatrix},$$

thus homogeneous shear barriers approach hyperbolic barriers as the length of the finite time interval $[t_0, t]$ tends to infinity. As for the steady center flow defined in (65), the shear vectors $\hat{\eta}_\pm$ are undefined since $\hat{\xi}_i$ are not well-defined. Therefore, as expected, this steady linear center flow admits no shear barriers either.

D.2. Example: Homogeneous transport barriers in unsteady parallel shear flows

In this example only, we use the usual Cartesian coordinates $(x, y) \in U$ and the velocity field coordinates (u, v) to simplify our notation. Consider the unsteady parallel shear flow

$$\dot{x} = u(y, t),$$
$$\dot{y} = v(t) \tag{68}$$

on a planar domain $(x, y) \in U$, with arbitrary time dependence in the velocities $u(y, t)$ and $v(t)$. We introduce the integrated Eulerian shear

$$a(y) = \int_{t_0}^t u_y(y, \tau)d\tau, \tag{69}$$

and assume that the time-averaged shear is non-vanishing ($a(y_0) \neq 0$) and nonlinear, i.e., $da(y)/dy$ does not vanish on any open subset of U.

The flow map, its gradient, and the Cauchy–Green strain tensor for (68) can be written as

$$F_{t_0}^t(x_0, y_0) = \begin{pmatrix} x_0 + \int_{t_0}^t u(y_0, \tau)d\tau \\ y_0 + \int_{t_0}^t v(\tau)d\tau \end{pmatrix},$$

$$DF_{t_0}^t(x_0, y_0) = \begin{pmatrix} 1 & a(y_0) \\ 0 & 1 \end{pmatrix},$$

$$C_{t_0}^t(x_0, y_0) = \begin{pmatrix} 1 & a(y_0) \\ a(y_0) & 1 + a^2(y_0) \end{pmatrix}.$$

The eigenvalues and eigenvectors of the tensor field $C_{t_0}^t$ satisfy

$$\lambda_1(y_0) = \frac{1}{2}a^2 + 1 - \frac{1}{2}a\sqrt{a^2+4},$$
$$\lambda_2(y_0) = \frac{1}{2}a^2 + 1 + \frac{1}{2}a\sqrt{a^2+4},$$
$$\xi_1(y_0) = \begin{pmatrix} \frac{a}{\sqrt{a^2+(\lambda_1-1)^2}} \\ \frac{\lambda_1 - 1}{\sqrt{a^2+(\lambda_1-1)^2}} \end{pmatrix},$$
$$\xi_2(y_0) = \begin{pmatrix} \frac{a}{\sqrt{a^2+(\lambda_2-1)^2}} \\ \frac{\lambda_2 - 1}{\sqrt{a^2+(\lambda_2-1)^2}} \end{pmatrix}.$$

Note that the minimum strain eigenvector $\xi_1(y_0)$ is constant along each $y = y_0$ line, and satisfies

$$\xi_1(y_0)\cdot\begin{pmatrix}0\\1\end{pmatrix} \neq 0, \qquad (x_0, y_0) \in U, \tag{70}$$

given that $\lambda_1(y_0) - 1 < 0$ holds for $a \neq 0$.

D.2.1. Cauchy–Green geodesics

In the Euler–Lagrange equations (20) corresponding to our example flow (68), all Christoffel symbols vanish, except for $\Gamma_{22}^1 = \frac{da}{dy_0}$. Therefore, the Cauchy–Green strain geodesics satisfy the equations

$$r_1'' + \frac{da(r_2(s))}{dy_0}\left(r_2'\right)^2 = 0, \tag{71}$$
$$r_2'' = 0.$$

Integrating these equations twice gives the general form of geodesics as

$$\begin{aligned} r_1(s) &= r_1(0) + \left[r_1'(0) + a(r_2(0))r_2'(0)\right]s \\ &\quad - r_2'(0)\int_0^s a(r_2(\sigma))d\sigma, \end{aligned} \tag{72}$$
$$r_2(s) = r_2(0) + r_2'(0)s.$$

D.2.2. Homogeneous hyperbolic barriers

For the geodesic $r(s)$ to satisfy the hyperbolic boundary condition (15), we must have

$$r'(s_{1,2}) \parallel \xi_1\left(r(s_{1,2})\right). \tag{73}$$

Combining (72) and (73) leads to the identity

$$\begin{aligned} &\frac{2a(r_2(0))}{a^2(r_2(0)) - \sqrt{a^4(r_2(0)) + 4a^2(r_2(0))}} + a(r_2(0)) \\ &\quad = \frac{2a(r_2(s))}{a^2(r_2(s)) - \sqrt{a^4(r_2(s)) + 4a^2(r_2(s))}} + a(r_2(s)). \end{aligned} \tag{74}$$

One may verify that the function $g(a) = \frac{2a}{a^2-\sqrt{a^4+4a^2}} + a$ is one-to-one, so condition (74) can only hold if $a(r_2(s)) = a(r_2(0))$. If $r(s)$ parametrizes a homogeneous geodesic, then $a(r_2(s)) \equiv a(r_2(0))$ must hold for any s, implying

$$\frac{da\left(r_2(s)\right)}{ds} = \frac{da\left(r_2(s)\right)}{dy_0}r_2'(s) = 0. \tag{75}$$

By our nonlinearity assumption ($da(y)/dy$ does not vanish on open subsets of U), we conclude from (75) that $r_2'(s) \equiv 0$ must hold on any geodesic that is a hyperbolic transport barrier. This, however, contradicts (73) because of the relation (70), therefore an unsteady parallel shear flow of the form (68) does not admit any hyperbolic transport barriers in the sense of Definition 2, as expected.

D.2.3. Homogeneous shear barriers

By formula (56) of Appendix A, the angle ϕ enclosed by the shear vectors and the x axis satisfies the equation

$$\sin\phi\left(2a\cos\phi + a^2\sin\phi\right) = 0,$$

yielding the solutions $\phi_1 = 0$ and $\phi_2 = \tan^{-1}(-2/a)$, or, equivalently, the shear vectors

$$\eta_+(y_0) = \begin{pmatrix}1\\0\end{pmatrix}, \qquad \eta_-(y_0) = \frac{1}{\sqrt{a^2+4}}\begin{pmatrix}a\\-2\end{pmatrix}. \tag{76}$$

Recall that a homogeneous shear barrier must be tangent to one of the vector fields $\eta_+(y_0)$ and $\eta_-(y_0)$. Assume first that $r'(s) \parallel \eta_-(y_0)$ holds. By (72), this would mean

$$2\left[\frac{r_1'(0)}{r_2'(0)} + a(r_2(0))\right] = a(r_2(s)), \tag{77}$$

where we also used the fact that $r_2'(0) \neq 0$ on a geodesic tangent to $\eta_-(r'(0))$. Differentiating (77) with respect to s again yields Eq. (75), and hence we obtain a contradiction with our assumption that $r'(s) \parallel \eta_-(y_0)$. Assuming $r'(s) \parallel \eta_+(y_0)$ instead, we obtain from (72) and (76) that the geodesics

$$r_1(s) = r_1(0) + r_1'(0)s,$$
$$r_2(s) = r_2(0),$$

are tangent to the η_+ vector field. We conclude that any horizontal line γ_0 marks the time-t_0 position of a homogeneous shear barrier in the shear flow (68). The corresponding evolving transport barriers γ_t can be obtained by integrating Eq. (68) from t_0 to t.

D.2.4. Jet cores

We now relax our initial assumptions and allow for the averaged shear to vanish at an isolated point, i.e., we assume for system (68) that for some value $\bar{y}$ of the vertical coordinate, we have

$$a(y) \neq 0, \quad y \neq \bar{y};$$
$$a(\bar{y}) = 0, \quad \frac{da(\bar{y})}{dy} \neq 0.$$

One can think of the zero shear line $y = \bar{y}$ as the core or a parallel jet. Away from this core, our analysis above applies and yields horizontal lines that act as homogeneous shear barriers. At $y_0 = \bar{y}$, however, we obtain

$$F_{t_0}^t(x_0, y_0) = \begin{pmatrix} x_0 + \int_{t_0}^t u(\bar{y}, \tau)d\tau \\ y_0 \end{pmatrix},$$
$$DF_{t_0}^t(x_0, \bar{y}) = \begin{pmatrix} 1 & 0 \\ 0 & 1 \end{pmatrix}, \qquad C_{t_0}^t(x_0, \bar{y}) = \begin{pmatrix} 1 & 0 \\ 0 & 1 \end{pmatrix},$$

respectively. Both eigenvalues of $C_{t_0}^t(x_0, \bar{y})$ are equal to one at these points and hence there is no uniquely defined larger or smaller strain eigenvector.

The only non-vanishing Christoffel symbol is still $\Gamma_{22}^1 = \frac{da}{dy_0}$, leading to the same Euler–Lagrange equation (71) and the same geodesics as in (72). The vast majority of these geodesics cross or avoid the jet core, and their subsets away from the jet core are covered by our prior analysis. An exception is the geodesic satisfying initial conditions of the form $r_2(0) = \bar{y}$, $r_2'(0) = 0$, for which (72) yields the full solution

$$r_1(s) = r_1(0) + r_1'(0)s$$
$$r_2(s) = \bar{y},$$

that remains inside the vertical line $y = \bar{y}$. This shows that even though the degeneracy of the jet core $y = \bar{y}$ prevents it from satisfying hyperbolic or shear boundary conditions, this core still is a Cauchy–Green geodesic.

Appendix E. Proof of Theorem 2

E.1. Proof of some strain eigenvector-field identities

First, we prove the identities

$$\begin{aligned}
&\nabla\xi_1\xi_1 = \kappa_1\xi_2, && (\nabla\xi_1)^T\xi_1 = 0,\\
&\nabla\xi_1\xi_2 = -\kappa_2\xi_2, && (\nabla\xi_1)^T\xi_2 = \kappa_1\xi_1 - \kappa_2\xi_2,\\
&\nabla\xi_2\xi_2 = \kappa_2\xi_1, && (\nabla\xi_2)^T\xi_2 = 0,\\
&\nabla\xi_2\xi_1 = -\kappa_1\xi_1, && (\nabla\xi_2)^T\xi_1 = \kappa_2\xi_2 - \kappa_1\xi_1,
\end{aligned} \tag{78}$$

where $\kappa_i(x)$ denotes the curvature of the trajectory of the ξ_i field at the point x, with respect to the unit normal ξ_j with $i \neq j$. These identities play a key role in the proof of geodesic deviation formulae for strainlines and shearlines.

Differentiation of the identity $\xi_1^j\xi_1^j = 1$ with respect to x^k, then subsequent multiplication by ξ_1^k yields the expressions

$$(\nabla\xi_1)^T\xi_1 = 0, \qquad (\nabla\xi_1)\xi_1 \perp \xi_1,$$

or, equivalently,

$$(\nabla\xi_1)^T\xi_1 = 0, \qquad (\nabla\xi_1)\xi_1 = \kappa_1\xi_2 \tag{79}$$

for an appropriate real-valued function $\kappa_1(x)$.

In addition to (79), we note two further identities that follow from $\langle\xi_i, \xi_i\rangle = 1$ by differentiation with respect to x then left-multiplication by ξ_j^T with $i \neq j$:

$$\begin{aligned}
&(\nabla\xi_2)^T\xi_2 = 0, \qquad (\nabla\xi_2)\xi_2 \perp \xi_2.\\
&\nabla\xi_1\xi_2 \parallel \xi_2, \qquad \nabla\xi_2\xi_1 \parallel \xi_1.
\end{aligned} \tag{80}$$

The second set of equations in (80) implies

$$\nabla\xi_1\xi_2 = \vartheta_1\xi_2, \qquad \nabla\xi_2\xi_1 = \vartheta_2\xi_1, \qquad \nabla\xi_2\xi_2 = \kappa_2\xi_1, \tag{81}$$

where ϑ_k denotes the single nonzero eigenvalue[8] of the Jacobian $\nabla\xi_k$ corresponding to its eigenvector ξ_j with $j \neq k$, and $\kappa_2(x)$ is an appropriate real-valued function.

Note that

$$\begin{aligned}
(\nabla\xi_1)^T\xi_2 &= \left\langle\xi_2, (\nabla\xi_1)^T\xi_2\right\rangle\xi_2 + \left\langle\xi_1, (\nabla\xi_1)^T\xi_2\right\rangle\xi_1\\
&= \langle\nabla\xi_1\xi_2, \xi_2\rangle\xi_2 + \langle\nabla\xi_1\xi_1, \xi_2\rangle\xi_1\\
&= \vartheta_1\xi_2 + \kappa_1\xi_1.
\end{aligned} \tag{82}$$

Equivalently, taking the gradient of the identity $\langle\xi_1, \xi_2\rangle = 0$, we obtain

$$\begin{aligned}
(\nabla\xi_1)^T\xi_2 &= -(\nabla\xi_2)^T\xi_1\\
&= \left\langle\xi_2, -(\nabla\xi_2)^T\xi_1\right\rangle\xi_2 + \left\langle\xi_1, -(\nabla\xi_2)^T\xi_1\right\rangle\xi_1\\
&= -\langle\nabla\xi_2\xi_2, \xi_1\rangle\xi_2 - \langle\nabla\xi_2\xi_1, \xi_1\rangle\xi_1\\
&= -\kappa_2\xi_2 - \vartheta_2\xi_1.
\end{aligned} \tag{83}$$

Comparing (82) and (83) gives the following relationships between κ_i and ϑ_j:

$$\vartheta_1 = -\kappa_2, \qquad \vartheta_2 = -\kappa_1,$$

leading to the final set of identities listed in (78).

It remains to show that $\kappa_i(x)$ is in fact the curvature of the trajectory of the ξ_i field at the point x, with respect to the unit normal ξ_j. Since a trajectory $r(s)$ of the vector field ξ_1 satisfies the differential equation $r'(s) = \xi_1(r(s))$, the classic formula for the curvature κ of this trajectory (see, e.g., [18]) with respect to its unit normal $\xi_2(r(s))$ yields

$$\kappa = \frac{\det(r', r'')}{|r'|^3} = \frac{\left\langle\xi_2, r''\right\rangle}{|\xi_1|^3} = \langle\xi_2, \nabla\xi_1\xi_1\rangle = \kappa_1, \tag{84}$$

as claimed, where we have used the fifth identity from (78), as well as formula (6) for the orientation of the strain eigenvectors. The proof for κ_2 being the curvature of the trajectories of the ξ_2 vector field is identical.

---

8 Observe that the other eigenvalue of $\nabla\xi_k$ is always zero because $(\nabla\xi_k)^T$ is a singular matrix, as seen from (79) and (80). The eigenvector corresponding to this zero eigenvalue is found to be $e_k = \kappa_k\xi_j - \nu_k\xi_k (j \neq k)$.

E.2. Proof of the geodesic deviation formulae (31) and (32) for strainlines

Here we compute the pointwise geodesic deviation $d_g^{\xi_1}$ for a strainline $\gamma_{t_0}(s)$. On a strainline, by definition, have $\gamma_{t_0}'(s_p) = r'(s_p) = \xi_1(p)$. Therefore, by the definition (27) of the geodesic deviation, the first term in (28) vanishes.

To evaluate the second term in (28), we differentiate the identity $\gamma_{t_0}'(s) = \xi_1(\gamma_{t_0}(s))$ to obtain

$$\gamma_{t_0}''(s_p) = \nabla\xi_1(p)\xi_1(p). \tag{85}$$

Furthermore, from the Euler–Lagrange equations (20), we have

$$r''(s_p) = G(p, \xi_1(p)),$$

with the function G defined in (29). This enables us to rewrite formula (28) for strainlines as

$$d_g^{\xi_1} = \left|\langle[\nabla\xi_1\xi_1 - G(r,\xi_1)], \xi_2\rangle\right|. \tag{86}$$

In order to evaluate (86) further, we first note the following identities that follow from the eigenvalue equation $C_{ij}\xi_1^j = \lambda_1\xi_1^i$:

$$C_{lj,k}\xi_1^j\xi_1^k = C_{lk,j}\xi_1^j\xi_1^k = \lambda_{1,k}\xi_1^k\xi_1^l + \lambda_1\xi_{1,k}^l\xi_1^k - C_{lj}\xi_{1,k}^j\xi_1^k, \tag{87}$$

$$C_{jk,l}\xi_1^j\xi_1^k = \lambda_{1,l}.$$

Next, using the definition of the function G in (29) along with the identities in (87), we obtain

$$G^i(r,\xi_1) = -C^{il}\left[\lambda_{1,k}\xi_1^k\xi_1^l + \lambda_1\xi_{1,k}^l\xi_1^k - C_{lj}\xi_{1,k}^j\xi_1^k - \frac{1}{2}\lambda_{1,l}\right]. \tag{88}$$

Using the identities (87) again, we find that the terms in the right-hand side of the expression (88) can be rewritten as

$$-C^{il}\lambda_{1,k}\xi_1^k\xi_1^l = -\frac{1}{\lambda_1}\lambda_{1,k}\xi_1^k\xi_1^i,$$

$$\begin{aligned}
-\lambda_1 C^{il}\xi_{1,k}^l\xi_1^k &= -\lambda_1\left(C^{jl}\xi_{1,k}^l\xi_1^k\xi_2^j\right)\xi_2^i - \lambda_1\left(C^{jl}\xi_{1,k}^l\xi_1^k\xi_1^j\right)\xi_1^i \\
&= -\frac{\lambda_1}{\lambda_2}\xi_{1,k}^l\xi_1^k\xi_2^l\xi_2^i - \left(\xi_{1,k}^l\xi_1^k\xi_1^l\right)\xi_1^i \\
&= -\frac{\lambda_1}{\lambda_2}\xi_{1,k}^l\xi_1^k\xi_2^l\xi_2^i,
\end{aligned}$$

$$C^{il}C_{lj}\xi_{1,k}^j\xi_1^k = \delta_j^i\xi_{1,k}^j\xi_1^k = \xi_{1,k}^i\xi_1^k,$$

$$\begin{aligned}
\frac{1}{2}C^{il}\lambda_{1,l} &= \frac{1}{2}\left[\left(C^{jl}\lambda_{1,l}\xi_1^j\right)\xi_1^i + \left(C^{jl}\lambda_{1,l}\xi_2^j\right)\xi_2^i\right] \\
&= \frac{1}{2\lambda_1}\lambda_{1,l}\xi_1^l\xi_1^i + \frac{1}{2\lambda_2}\lambda_{1,l}\xi_2^l\xi_2^i.
\end{aligned} \tag{89}$$

Based on these identities and those in (78), the function G defined in (88) can be written in the coordinate-free form

$$\begin{aligned}
G(r,\xi_1) &= -\frac{1}{2\lambda_1}\langle\nabla\lambda_1,\xi_1\rangle\xi_1 - \kappa_1\frac{\lambda_1}{\lambda_2}\xi_2 + \kappa_1\xi_2 \\
&\quad + \frac{1}{2\lambda_2}\langle\nabla\lambda_1,\xi_2\rangle\xi_2.
\end{aligned} \tag{90}$$

Substituting (90) into the geodesic deviation formula (86), we obtain

$$d_g^{\xi_1} = \left|\langle[\nabla\xi_1\xi_1 - G(r,\xi_1)], \xi_2\rangle\right| \tag{91}$$

$$= \frac{1}{\lambda_2}\left|\lambda_1\kappa_1 - \frac{1}{2}\langle\nabla\lambda_1,\xi_2\rangle\right|, \tag{92}$$

which proves formula (31).

Consider now an incompressible flow ($\nabla\cdot v = 0$) in (1). For such flows, (38) yields the relationships

$$\lambda_1 = \frac{1}{\lambda_2}, \qquad \nabla\lambda_1 = -\frac{\lambda_1}{\lambda_2}\nabla\lambda_2 = -\frac{1}{\lambda_2^2}\nabla\lambda_2. \tag{93}$$

These formulae allow us to rewrite (91) as (32).

E.3. Proof of the geodesic deviation formulae (33) and (34) for shearlines

Here we compute the pointwise geodesic deviation $d_g^{\eta\pm}$ for a shearline $\gamma_{t_0}(s)$. By the definition of shearlines, we have

$$\gamma_{t_0}' = \eta_\pm(\gamma_{t_0}) = \alpha(\gamma_{t_0})\xi_1(\gamma_{t_0}) \pm \beta(\gamma_{t_0})\xi_2(\gamma_{t_0}), \tag{94}$$

$$\alpha = \sqrt{\frac{\sqrt{\lambda_2}}{\sqrt{\lambda_1}+\sqrt{\lambda_2}}}, \qquad \beta = \sqrt{\frac{\sqrt{\lambda_1}}{\sqrt{\lambda_1}+\sqrt{\lambda_2}}}.$$

Differentiation of the above differential equation with respect to s gives

$$\begin{aligned}
\gamma_{t_0}'' &= \langle\nabla\alpha,\eta_\pm\rangle\xi_1 + \alpha\nabla\xi_1\eta_\pm \pm \langle\nabla\beta,\eta_\pm\rangle\xi_2 \pm \beta\nabla\xi_2\eta_\pm \\
&= \langle\nabla\alpha,\eta_\pm\rangle\xi_1 + \alpha^2\kappa_1\xi_2 \mp \alpha\beta\kappa_2\xi_2 \pm \langle\nabla\beta,\eta_\pm\rangle\xi_2 \\
&\quad + \beta^2\kappa_2\xi_1 \mp \alpha\beta\kappa_1\xi_1.
\end{aligned} \tag{95}$$

As a result, we have

$$\begin{aligned}
\left\langle\gamma_{t_0}'', \Omega\gamma_{t_0}'\right\rangle &= \big\langle\big[\langle\nabla\alpha,\eta_\pm\rangle\xi_1 + \alpha^2\kappa_1\xi_2 \\
&\qquad \mp \alpha\beta\kappa_2\xi_2 \pm \langle\nabla\beta,\eta_\pm\rangle\xi_2 \\
&\qquad + \beta^2\kappa_2\xi_1 \mp \alpha\beta\kappa_1\xi_1\big], (\mp\beta\xi_1 + \alpha\xi_2)\big\rangle \\
&= \mp\beta\langle\nabla\alpha,\eta_\pm\rangle + \alpha^3\kappa_1 \\
&\quad \mp \alpha^2\beta\kappa_2 \pm \alpha\langle\nabla\beta,\eta_\pm\rangle \mp \beta^3\kappa_2 + \alpha\beta^2\kappa_1 \\
&= \mp\langle\beta\nabla\alpha - \alpha\nabla\beta,\eta_\pm\rangle + \alpha\kappa_1 \mp \beta\kappa_2 \\
&= \mp\frac{1}{\beta}\langle\nabla\alpha,\eta_\pm\rangle + \alpha\kappa_1 \mp \beta\kappa_2,
\end{aligned} \tag{96}$$

where we have used the identity $\alpha^2 + \beta^2 = 1$, as well as its consequence, $\nabla\beta = -(\alpha/\beta)\nabla\alpha$. Substitution of (95) into the simplified geodesic deviation formula (28) gives

$$\begin{aligned}
d_g^{\eta\pm} &= |1 - \langle\eta_\pm,\xi_1\rangle| + \left|\left\langle\gamma_{t_0}'',\Omega\gamma_{t_0}'\right\rangle - \langle G(p,\xi_1),\xi_2\rangle\right| \\
&= |1-\alpha| + \left|\mp\frac{1}{\beta}\langle\nabla\alpha,\eta_\pm\rangle + \alpha\kappa_1 \mp \beta\kappa_2\right. \\
&\quad \left. + \left(\frac{\lambda_1}{\lambda_2} - 1\right)\kappa_1 - \frac{1}{2\lambda_2}\langle\nabla\lambda_1,\xi_2\rangle\right|,
\end{aligned} \tag{97}$$

proving formula (33).

For incompressible flows, the relationships (93) again hold between λ_1, λ_2 and their gradients. Furthermore, the coefficients α and β simplify to

$$\alpha = \frac{1}{\sqrt{1+\lambda_1}}, \qquad \beta = \frac{1}{\sqrt{1+\lambda_2}}. \tag{98}$$

Using these relations in the terms appearing on the right-hand side of (97), we obtain

$$\begin{aligned}
\mp\frac{1}{\beta}\langle\nabla\alpha,(\alpha\xi_1 \pm \beta\xi_2)\rangle &= \pm\frac{\sqrt{1+\lambda_2}\langle\nabla\lambda_1,\xi_1\rangle}{2(1+\lambda_1)} + \frac{\langle\nabla\lambda_1,\xi_2\rangle}{2\sqrt{1+\lambda_1}^3} \\
&= \mp\frac{\langle\nabla\lambda_2,\xi_1\rangle}{2\lambda_2\sqrt{1+\lambda_2}} - \frac{\langle\nabla\lambda_2,\xi_2\rangle}{2\sqrt{\lambda_2}\sqrt{1+\lambda_2}^3},
\end{aligned}$$

$$\alpha\kappa_1 = \frac{\kappa_1}{\sqrt{1+\lambda_1}} = \frac{\kappa_1\sqrt{\lambda_2}}{\sqrt{1+\lambda_2}}$$

$$\mp\beta\kappa_2 = \mp\frac{\kappa_2}{\sqrt{1+\lambda_2}}.$$

Substituting these expressions into (97), we obtain

$$\begin{aligned}
d_g^{\eta\pm} &= \left|\frac{\sqrt{1+\lambda_1}-1}{\sqrt{1+\lambda_1}}\right| + \left|\mp\frac{\langle\nabla\lambda_2,\xi_1\rangle}{2\lambda_2\sqrt{1+\lambda_2}}\right. \\
&\quad - \frac{\langle\nabla\lambda_2,\xi_2\rangle}{2\sqrt{\lambda_2}\sqrt{1+\lambda_2}^3} + \frac{\kappa_1\sqrt{\lambda_2}}{\sqrt{1+\lambda_2}} \mp \frac{\kappa_2}{\sqrt{1+\lambda_2}}
\end{aligned}$$

$$+\left(\frac{1}{\lambda_2^2}-1\right)\kappa_1+\frac{1}{2\lambda_2^3}\langle\nabla\lambda_2,\xi_2\rangle\Bigg|$$

$$=\frac{\sqrt{1+\lambda_2}-\sqrt{\lambda_2}}{\sqrt{1+\lambda_2}}+\Bigg|\mp\frac{\langle\nabla\lambda_2,\xi_1\rangle}{2\lambda_2\sqrt{1+\lambda_2}}$$

$$+\frac{\langle\nabla\lambda_2,\xi_2\rangle\left(\sqrt{1+\lambda_2}^3-\sqrt{\lambda_2}^5\right)}{2\lambda_2^3\sqrt{1+\lambda_2}^3}$$

$$+\frac{\kappa_1\left[\sqrt{\lambda_2}^5+(1-\lambda_2^2)\sqrt{1+\lambda_2}\right]}{\lambda_2^2\sqrt{1+\lambda_2}}\mp\frac{\kappa_2}{\sqrt{1+\lambda_2}}\Bigg|,$$

which proves formula (34).

E.4. Proof of the general geodesic deviation formula (35)

At a point $\gamma_{t_0}(s)$ of a general transport barrier candidate, the curvature κ of $\gamma_{t_0}(s)$ and the curvature κ_0 of the locally least-stretching geodesic $r(s)$ can be written in index notation as

$$\begin{aligned}\kappa&=\frac{\det(\gamma_{t_0}',\gamma_{t_0}'')}{|\gamma_{t_0}'|^3}=\frac{\langle\gamma_{t_0}'',\Omega\gamma_{t_0}'\rangle}{|\gamma_{t_0}'|^3}=\frac{1}{|\gamma_{t_0}'|^3}\Omega_{ij}\left(\gamma_{t_0}^i\right)''\left(\gamma_{t_0}^j\right)',\\ \kappa_0&=\frac{\det(r',r'')}{|r'|^3}=\frac{\langle r'',\Omega r'\rangle}{|r'|^3}=\frac{1}{|r'|^3}\Omega_{ij}\left(r^i\right)''\left(r^j\right)'.\end{aligned}\tag{99}$$

The explicit solution (24) enables us to evaluate r''. Specifically, writing (24) in index form, using the shorthand notation F_i for the ith coordinate function of the flow map $F_{t_0}^t$, differentiating (24) twice with respect to s, and setting $s=0$, we obtain

$$\left(r^i\right)''=F_{i,jl}^{-1}F_{l,m}\left(r_{EL}^m\right)'F_{j,k}\left(r_{EL}^k\right)'.$$

Using the index notation $F^{i,j}$ for the tensor $\left[DF_{t_0}^t\right]^{-1}$, and noting that $r'=\xi_1$ holds on the locally least-stretching geodesic, we obtain

$$\left(r^i\right)''=F^{i,jl}F_{j,k}F_{l,m}\left(\xi_1^k\right)'\left(\xi_1^m\right)'.\tag{100}$$

Using (99) and (100), we obtain the curvature difference

$$\kappa-\kappa_0=\Omega_{ij}\left[\frac{\left(\gamma_{t_0}^i\right)''\left(\gamma_{t_0}^j\right)'}{\left[\left(\gamma_{t_0}^i\right)'\left(\gamma_{t_0}^i\right)'\right]^{3/2}}-F^{i,jl}F_{j,k}F_{l,m}\left(\xi_1^k\right)'\left(\xi_1^m\right)'\left(\xi_1^j\right)'\right].\tag{101}$$

Substituting (101) into the second term $|\kappa-\kappa_0|$ of the geodesic deviation formula (27) gives

$$\begin{aligned}d_g&=\left|1-\frac{\langle\gamma_{t_0}',\xi_1\rangle}{|\gamma_{t_0}'|}\right|+|\kappa-\kappa_0|\\&=\left|1-\frac{\left(\gamma_{t_0}^i\right)'\xi_1^i}{|\gamma_{t_0}'|}\right|+\left|\Omega_{ij}\left[\frac{\left(\gamma_{t_0}^i\right)''\left(\gamma_{t_0}^j\right)'}{|\gamma_{t_0}'|^{3/2}}-F^{i,jl}F_{j,k}F_{l,m}\left(\xi_1^k\right)'\left(\xi_1^m\right)'\left(\xi_1^j\right)'\right]\right|,\end{aligned}$$

which proves formula (35).

Appendix F. Proof of Proposition 2

Let γ_{t_0} be a compact shearline, and let $\gamma_{t_0}(s)$ be its parametrization by arclength. We then have

$$\gamma_{t_0}'(s)=z(\gamma_{t_0}(s))\eta_\pm(\gamma_{t_0}(s)),\tag{102}$$

where the function $z(\gamma_{t_0}(s))$ takes discrete values from the set $\{-1,1\}$, and is introduced to eliminate any potential orientational discontinuity of the shear vector field (cf. Section 7.3). Using formulae (3) and (18), and recalling that $\lambda_1\lambda_2=1$ holds for incompressible flows, we can write the length of the material curve $\gamma_{t_0+T}=F_{t_0}^{t_0+T}(\gamma_0)$ as

$$\begin{aligned}l(\gamma_{t_0+T})&=\int_0^{l(\gamma_{t_0})}\sqrt{\left\langle\gamma_{t_0}'(s)C_{t_0}^{t_0+T}\left(\gamma_{t_0}(s)\right)\gamma_{t_0}'(s)\right\rangle}ds\\&=\int_0^{l(\gamma_0)}\left|z(\gamma_{t_0}(s))\right|\sqrt{\lambda_1\left(\gamma_{t_0}(s)\right)\lambda_2\left(\gamma_{t_0}(s)\right)}ds\\&=\int_0^{l(\gamma_{t_0})}ds=l(\gamma_{t_0}),\end{aligned}$$

which proves Proposition 2.

Appendix G. Extension to two-dimensional flows over smooth surfaces

Here we show how our approach to transport barriers in planar flows extends to flows defined on two-dimensional surfaces, such as geophysical flows.

Let a two-dimensional smooth surface M be embedded in the Euclidean space $\mathbb{R}^3$ through a local parametrization $f:x\mapsto f(x)\in M$, with $x\in U\in\mathbb{R}^2$ denoting two-dimensional local coordinates for M. We assume that the flow of interest is given in terms of the x coordinates, satisfying a differential equation of the form

$$\dot{x}=v(x,t).\tag{103}$$

For instance, $x=(\phi,\theta)$ can be longitudinal and latitudinal coordinates of a sphere, whose dimension is angle, as opposed to length. In that case, the field $v(x,t)$ is a vector of angular velocities. The flow map associated with (103) is also two-dimensional, defined again as $F_{t_0}^t:x_0\mapsto x(t;t_0,x_0)$.

Assume that the initial curve $\gamma_0\in U$ is parametrized by the function $r(s)$ at time t_0. The curve γ_0 is advected by the flow map $F_{t_0}^t$, generating a material line $\gamma_t=F_{t_0}^t(\gamma_0)$ in the space of the local coordinates of M. This curve in the coordinate space U generates a curve $f(\gamma_t)$ on M (see Fig. 25), whose length can be measured using the standard Euclidean inner product inherited by M from the ambient space $\mathbb{R}^3$

$$\begin{aligned}l_M(\gamma_t)&=\int_{s_1}^{s_2}\sqrt{\left|\frac{d}{ds}f\left(F_{t_0}^t(r(s))\right)\right|^2}ds\\&=\int_{s_1}^{s_2}\sqrt{\left\langle r'(s),\tilde{C}_{t_0}^t(r(s))r'(s)\right\rangle}ds,\end{aligned}\tag{104}$$

where the two-dimensional, positive semi-definite tensor field $\tilde{C}_{t_0}^t$ is defined as

$$\begin{aligned}\tilde{C}_{t_0}^t(x_0)&=\left[DF_{t_0}^t(x_0)\right]^T G(F_{t_0}^t(x_0))DF_{t_0}^t(x_0),\\ G(x)&=[Df(x)]^T Df(x).\end{aligned}\tag{105}$$

Here $G(x)$ is the representation of the metric tensor of M in terms of the local coordinate x, and Df denotes the Jacobian of the local parametrization f.[9] In differential geometric terms, $\tilde{C}_{t_0}^t(x_0)$ is the tensor generating the pull-back metric $\tilde{c}=\left(f\circ F_{t_0}^t\right)^*e$ on the coordinate space $U\subset\mathbb{R}^2$, with e denoting the Riemannian metric on $\mathbb{R}^3$ (see, e.g., [35]).

[9] To avoid technicalities with switching between different local parametrizations of M, we have assume here that $|t-t_0|$ is small enough so that γ_t also lies in U. Alternatively, we may also assume that the function f in fact provides a global parametrization of M.

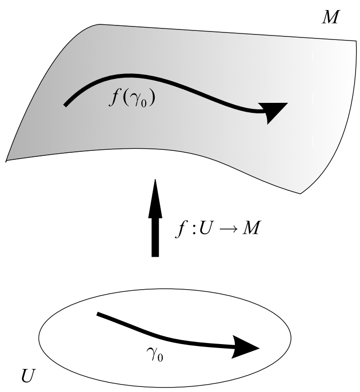

Fig. 25. Set-up for extension to flows on two-dimensional surfaces.

We define the length functional $l_{t_0}^t$ of the initial material line position γ_0 to be equal to the stretched length of γ_t, as measured in the metric of the actual flow domain, the surface M:

$$l_{t_0}^t(\gamma_0) := l_M(\gamma_t).$$

By analogy between Eqs. (3) and (104), all our results on transport barriers remain valid if we use the pull-back Cauchy–Green strain tensor $\tilde{C}_{t_0}^t(x_0)$ instead of the classic Cauchy–Green strain tensor $C_{t_0}^t(x_0)$.

G.1. Example: Transport barriers in flow over a sphere

Assume that the surface M is a two-dimensional sphere of radius r embedded in $\mathbb{R}^3$. In spherical polar coordinates, points on M are parametrized as

$$f(\phi,\theta) = \begin{pmatrix} r\sin\theta\cos\phi \\ r\sin\theta\sin\phi \\ r\cos\theta \end{pmatrix} \in \mathbb{R}^3.$$

The Jacobian of this function, and the corresponding induced metric tensor on M are of the form

$$Df(\phi,\theta) = \begin{pmatrix} -r\sin\theta\sin\phi & r\cos\theta\cos\phi \\ r\sin\theta\cos\phi & r\cos\theta\sin\phi \\ 0 & -r\sin\theta \end{pmatrix}, \qquad (106)$$
$$G(\phi,\theta) = [Df(\phi,\theta)]^T Df(\phi,\theta) = \begin{pmatrix} r^2\sin^2\theta & 0 \\ 0 & r^2 \end{pmatrix}.$$

Assume that an unsteady flow on the surface of the sphere is described in terms of the differential equations

$$\dot{\phi} = \omega_1(\phi,\theta,t),$$
$$\dot{\theta} = \omega_2(\phi,\theta,t),$$

generating the flow mapping and deformation gradient

$$F_{t_0}^t(\phi_0,\theta_0) = \begin{pmatrix} \phi(t;t_0,\phi_0,\theta_0) \\ \theta(t;t_0,\phi_0,\theta_0) \end{pmatrix},$$
$$DF_{t_0}^t(\phi_0,\theta_0) = \begin{pmatrix} \dfrac{\partial\phi(t;t_0,\phi_0,\theta_0)}{\partial\phi_0} & \dfrac{\partial\phi(t;t_0,\phi_0,\theta_0)}{\partial\theta_0} \\ \dfrac{\partial\theta(t;t_0,\phi_0,\theta_0)}{\partial\phi_0} & \dfrac{\partial\theta(t;t_0,\phi_0,\theta_0)}{\partial\theta_0} \end{pmatrix}. \qquad (107)$$

Then by formulae (105)–(107), all results in the earlier sections of this paper will apply in the spherical coordinates (ϕ,θ), provided we use the pull-back Cauchy–Green strain tensor

$$\tilde{C}_{t_0}^t(\phi_0,\theta_0) = \begin{pmatrix} \dfrac{\partial\phi(t;t_0,\phi_0,\theta_0)}{\partial\phi_0} & \dfrac{\partial\theta(t;t_0,\phi_0,\theta_0)}{\partial\phi_0} \\ \dfrac{\partial\phi(t;t_0,\phi_0,\theta_0)}{\partial\theta_0} & \dfrac{\partial\theta(t;t_0,\phi_0,\theta_0)}{\partial\theta_0} \end{pmatrix}$$
$$\times \begin{pmatrix} r^2\sin^2\theta(t;t_0,\phi_0,\theta_0) & 0 \\ 0 & r^2 \end{pmatrix}$$
$$\times \begin{pmatrix} \dfrac{\partial\phi(t;t_0,\phi_0,\theta_0)}{\partial\phi_0} & \dfrac{\partial\phi(t;t_0,\phi_0,\theta_0)}{\partial\theta_0} \\ \dfrac{\partial\theta(t;t_0,\phi_0,\theta_0)}{\partial\phi_0} & \dfrac{\partial\theta(t;t_0,\phi_0,\theta_0)}{\partial\theta_0} \end{pmatrix}.$$

References

[1] J.B. Weiss, A. Provenzale (Eds.), Transport and Mixing in Geophysical Flows, in: Lecture Notes in Physics, vol. 744, Springer, New York, 2008.
[2] J.M. Ottino, The Kinematics of Mixing: Stretching, Chaos, and Transport, Cambridge University Press, Cambridge, 1989.
[3] J.E. Marsden, S.D. Ross, New methods in celestial mechanics and mission design, Bull. Amer. Math. Soc. 43 (2006) 43–73.
[4] M. Toda, T. Komatsuzaki, T. Konishi, R.S. Berry, S.A. Rice (Eds.), Geometrical Structures of Phase Space in Multi-Dimensional Chaos: Applications to Chemical Reaction Dynamics in Complex Systems, Wiley-Interscience, 2005.
[5] L.C. Woods, Theory of Tokamak Transport: New Aspects for Nuclear Fusion Reactor Design, Wiley, 2006.
[6] J. Jeong, F. Hussain, On the identification of a vortex, J. Fluid Mech. 285 (1995) 69–94.
[7] G. Boffetta, G. Lacorata, G. Redaelli, A. Vulpiani, Detecting barriers to transport: a review of different techniques, Physica D 159 (2001) 58–70.
[8] G. Haller, An objective definition of a vortex, J. Fluid Mech. 525 (2005) 1–26.
[9] Peacock T., Dabiri J. (Eds.), Focus issue on Lagrangian coherent structures, Chaos 20 (2010).
[10] C. Basdevant, T. Philipovitch, On the validity of the "Weiss criterion" in two-dimensional turbulence, Physica D 73 (1994) 17–30.
[11] G. Haller, A variational theory of hyperbolic Lagrangian coherent structures, Physica D 240 (2011) 574–598.
[12] G. Froyland, N. Santitissadeekorn, A. Monahan, Transport in time-dependent dynamical systems: finite-time coherent sets, Chaos 20 (2010) 043116.
[13] M.R. Allshouse, J.-L. Thiffeault, Detecting coherent structures using braids, Physica D 241 (2012) 95–105.
[14] C. Truesdell, W. Noll, The Non-Linear Field Theories of Mechanics, Springer, New York, 2004.
[15] T. Delmarcelle, L. Hesselink, The topology of symmetric, second order tensor field, in: Proc. of Visualization'94, 1994, pp. 140–147.
[16] I.A. Gelfand, S.V. Fomin, Calculus of Variations, Dover Publications, 2000.
[17] J. Jost, Riemannian Geometry and Geometric Analysis, Springer, Berlin, 2002.
[18] P.A. Blaga, Lectures on the Differential Geometry of Curves and Surfaces, Napoca Press, 2005.
[19] V.I. Arnold, Mathematical Methods of Classical Mechanics, Springer, NY, 1978.
[20] M. Farazmand, G. Haller, Computing Lagrangian coherent structures from variational LCS theory, Chaos 22 (2012) 013128.
[21] K. Tchon, J. Dompierre, M.G. Vallet, F. Guibault, R. Camarero, Two-dimensional metric tensor visualization using pseudo-meshes, Eng. Comput. 22 (2006) 121–131.
[22] R. Calleja, R. de la Llave, Fast numerical computation of quasi-periodic equilibrium states in 1D statistical mechanics, including twist maps, Nonlinearity 22 (2009) 1311–1336.
[23] R.T. Pierrehumbert, Large-scale horizontal mixing in planetary atmospheres, Phys. Fluids A 3 (1991) 1250–1260.
[24] F.J. Beron-Vera, M.J. Olascoaga, M.G. Brown, H. Koçak, I.I. Rypina, Invariant-tori-like Lagrangian coherent structures in geophysical flows, Chaos 20 (2010) 017514.
[25] W.G. Bickley, The plane jet, Philos. Mag. 23 (1937) 727–731.
[26] D. del Castillo-Negrete, P.J. Morrison, Chaotic transport by Rossby waves in shear flow, Phys. Fluids A 5 (1993) 948–965.
[27] M.J. Olascoaga, G. Haller, Forecasting major instabilities in environmental contamination patterns, Proc. Natl. Acad. Sci. 109 (2012) 4738–4743.
[28] R.S. MacKay, J.D. Meiss, I.C. Percival, Transport in Hamiltonian systems, Physica D 13 (1984) 55–81.
[29] V. Rom-Kedar, S. Wiggins, Transport in two-dimensional maps, Arch. Ration. Mech. Anal. 109 (1990) 239–298.
[30] S. Wiggins, Chaotic Transport in Dynamical Systems, Springer, New York, 1992.
[31] C. Garth, F. Gerhardt, X. Tricoche, H. Hans, Efficient computation and visualization of coherent structures in fluid flow applications, IEEE Trans. Vis. Comput. Graphics 13 (2007) 1464–1471.
[32] C. Conti, D. Rossinelli, P. Koumoutsakos, GPU and APU computations of finite time Lyapunov exponent fields, J. Comput. Phys. 231 (2012) 2229–2244.
[33] W. Tang, P.W. Chan, G. Haller, Lagrangian coherent structure analysis of terminal winds detected by LIDAR. Part I: turbulence structures, J. Appl. Meteorol. Climatol. 50 (2011) 325–338.
[34] J. Moser, Selected Chapters in the Calculus of Variations, Birkhäuser, 2003.
[35] R. Abraham, J.E. Marsden, Foundations of Mechanics, Addison-Wesley, 1978.
[36] D.D. Holm, Geometric Mechanics Part I: Dynamics and Symmetry, Imperial College Press, London, 2011.